ANNUAL REVIEWS

Annual Review of Astronomy and Astrophysics

Advances in Optical/Infrared Interferometry

Frank Eisenhauer,[1] John D. Monnier,[2] and Oliver Pfuhl[3]

[1]Max Planck Institute for Extraterrestrial Physics, Garching, Germany; email: eisenhau@mpe.mpg.de

[2]Astronomy Department, University of Michigan, Ann Arbor, Michigan, USA; email: monnier@umich.edu

[3]European Southern Observatory, Garching, Germany; email: opfuhl@eso.org

Annu. Rev. Astron. Astrophys. 2023. 61:237–85

First published as a Review in Advance on June 7, 2023

The *Annual Review of Astronomy and Astrophysics* is online at astro.annualreviews.org

https://doi.org/10.1146/annurev-astro-121622-045019

Keywords

instrumentation, Galactic Center, exoplanets, active galactic nuclei, young stellar objects, stars

Abstract

After decades of fast-paced technical advances, optical/infrared (O/IR) interferometry has seen a revolution in recent years:

- The GRAVITY instrument at the Very Large Telescope Interferometer (VLTI) with four 8-m telescopes reaches thousand-times-fainter objects than possible with earlier interferometers, and the Center for High Angular Resolution Astronomy array (CHARA) routinely offers up to 330-m baselines and aperture synthesis with six 1-m telescopes.
- The observed objects are fainter than 19 mag, the images have sub-milliarcsecond resolution, and the astrometry reaches microarcsecond precision.
- This led to breakthrough results on the Galactic Center, exoplanets, active galactic nuclei, young stellar objects, and stellar physics.

Following a primer in interferometry, we summarize the advances that led to the performance boost of modern interferometers:

- Single-mode beam combiners now combine up to six telescopes, and image reconstruction software has advanced over earlier developments for radio interferometry.
- With a combination of large telescopes, adaptive optics (AO), fringe tracking, and especially dual-beam interferometry, GRAVITY has boosted the sensitivity by many orders of magnitude.

Another order-of-magnitude improvement will come from laser guide star AO. In combination with large separation fringe tracking, O/IR interferometry will then provide complete sky coverage for observations in the Galactic plane and substantial coverage for extragalactic targets.

Contents

1. INTRODUCTION

Optical and infrared (IR) interferometry is experiencing tremendous advances from leaps in sensitivity, precision, angular resolution, longer baselines, and better imaging. In this review, we present the technical and scientific achievements in optical/IR (O/IR) interferometry from roughly the past decade. We focus on the two main science-producing O/IR interferometers in the world, the European Southern Observatory (ESO)'s Very Large Telescope Interferometer (VLTI), in particular GRAVITY, and the Georgia State University Center for High Angular Resolution Astronomy array (CHARA). In addition, the Large Binocular Telescope Interferometer (LBTI) and the Navy Precision Optical Interferometer (NPOI) are discussed briefly.

Earlier reviews by Quirrenbach (2001) and Monnier (2003) thoroughly discussed the history of O/IR interferometry. More recently, a number of textbooks (Glindemann 2011, Labeyrie et al. 2014, Buscher 2015) have been introduced that augment the classic radio interferometry textbook from Thompson et al. (2017). We refer the reader to these sources for details beyond our cursory treatment. In this introduction, we give a short history of the field, make comparisons to the more familiar radio interferometry, and motivate the reasons for the recent performance increases.

1.1. Short History of Optical/Infrared Interferometry

The history of O/IR interferometry can be divided into three periods: The classical period from 1868 to 1930, the early-modern period from 1956 to 2005, and the modern "present" day from ~2000 to now. In this review, we propose that the fourth era has begun, one marked by GRAVITY and dual-beam phase referencing on 8- to 10-m-class telescopes that truly revolutionizes O/IR interferometry sensitivity.

Dual-beam phase referencing: technique to allow long coherent fringe integrations of a faint target by real-time fringe tracking of a bright nearby reference star

The earliest period is rooted firmly in nineteenth-century classical physics. Fizeau (1868) laid the foundation for how interference could be used to measure the sizes of stars by dividing the pupil of a telescope into small subapertures. The light from each pair of subapertures creates an interference pattern called a fringe, the basic result of a Young's two-slit interference experiment. In this arrangement, each point source creates its own sinusoidal fringe pattern; thus, an extended object creates a low-contrast interference as the peaks and troughs partially overlap to blur out the dark and destructive nulls present for point sources. Later, Stephan (1874) attempted on-sky experiments but was not able to resolve any stars. The effective angular resolution of an interferometer θ is defined as half the fringe spacing, $\theta = \frac{\lambda}{2B}$, expressed in radians for a wavelength λ and a baseline between subapertures of B.

Soon after Fizeau's and Stephan's pioneering work, Michelson developed a more thorough mathematical treatment, including coining the term fringe visibility to describe the coherence—with a visibility of unity corresponding to a perfect fringe with 100% destructive interference at the fringe troughs and with a zero visibility for no interference at all. Michelson first deployed this method to measure the sizes of Jupiter's moons (Michelson 1891), eventually resolving Betelgeuse at 47 mas using a 20-ft interferometer on top of the Mt. Wilson 100-in telescope (Michelson & Pease 1921). This "classical" period ends with the largely unsuccessful experiments to build the first truly long-baseline (50-ft) interferometer (Pease 1930).

Fringe visibility, $\tilde{V}$: complex number representing amplitude and phase of a fringe for a single interferometer baseline

Heterodyne interferometry: telescope light is first mixed with a local oscillator to create lower-frequency signals that can be interfered; used in radio

Direct detection: light beams are brought together and interfered at the time of photon detection; used in optical/infared

Aperture synthesis: technique to produce images with an array of telescopes as if coming from a much larger single-aperture telescope

The early-modern period of O/IR interferometry picks up with advances in electronics, optics, and detectors. The earliest revivals of long-baseline interferometry exploited new technologies, such as intensity interferometry (Brown & Twiss 1956, Hanbury Brown et al. 1967) and heterodyne interferometry in the mid-IR (MIR) by Nobel physicist Charles Townes (e.g., Johnson et al. 1974). Following pioneering work by Labeyrie (1975), early "direct detection" interferometers, such as the Mark III (Shao et al. 1988), I2T (Koechlin & Rabbia 1985), IRMA (Infrared Michelson Array; Dyck et al. 1993), and others (di Benedetto & Conti 1983), emerged and established the principles of our modern facilities, where light beams are collected at widely separated telescopes, often transported through vacuum pipes, brought into coherence using moving delay lines, and finally interfered directly on a detector.

Many of the projects in the 1980s and 1990s led directly to second-generation facilities: Narrabri Stellar Intensity Interferometer became SUSI (Sydney University Stellar Interferometer; Davis et al. 1999), McMath heterodyne interferometer became ISI (Infrared Spatial Interferometer; Hale et al. 2000), I2T (Interféromètre a 2 Télescopes) became GI2T (Grand Interféromètre a 2 Télescopes; Mourard et al. 1994), Mark III became NPOI (Armstrong et al. 1998) + PTI (Palomar Testbed Interferometer; Colavita et al. 1999), aperture masking became COAST (Cambridge Optical Aperture Synthesis Telescope; Baldwin et al. 1994), and IRMA became IOTA (Infrared Optical Telescope Array; Traub et al. 2003). Although all facilities from this era, except for NPOI, have been shut down, their collective technical impact has been impressive, setting the stage for the modern age.

The third, so-called modern era starts with the debut of the flagship facilities VLTI (Léna 1979, Beckers et al. 1990, Schöller 2007), NASA Keck Interferometer (KI; Colavita et al. 2013), CHARA (ten Brummelaar et al. 2005), and LBTI (Defrère et al. 2016), along with the evolution of NPOI. All of these facilities (except for the KI) are still operating as of 2022. See **Figure 1** for the physical layout of these arrays. The only major facility under construction today is the Magdalena Ridge Optical Interferometer (MROI; Buscher et al. 2013), which aims at combining up to ten 1.4-m telescopes over 350-m baselines. Within the past decade, no new interferometers have come online. For a more historical perspective of O/IR interferometry, see the timeline explored by Lawson (2000a) as well as the treatments by Léna (2020) and McAlister (2020).

1.2. Comparison with Radio Interferometry

Even the largest, single radio telescopes of the twentieth century barely reach the angular resolution of Galileo's first optical telescope from 1609. There is no practical way to build single telescopes large enough to sufficiently reduce the diffraction of the long radio wavelengths. Therefore, ever since the development in the 1950s, aperture synthesis interferometry (Jennison 1958, Ryle & Hewish 1960) has been the standard choice for high angular resolution telescopes in the microwave and radio bands (Thompson et al. 2017). Why has this not been the case in O/IR astronomy?

The principle of radio aperture synthesis interferometry is to measure the correlated flux from a celestial source on a number of baselines, each with two antennas, for different baseline length

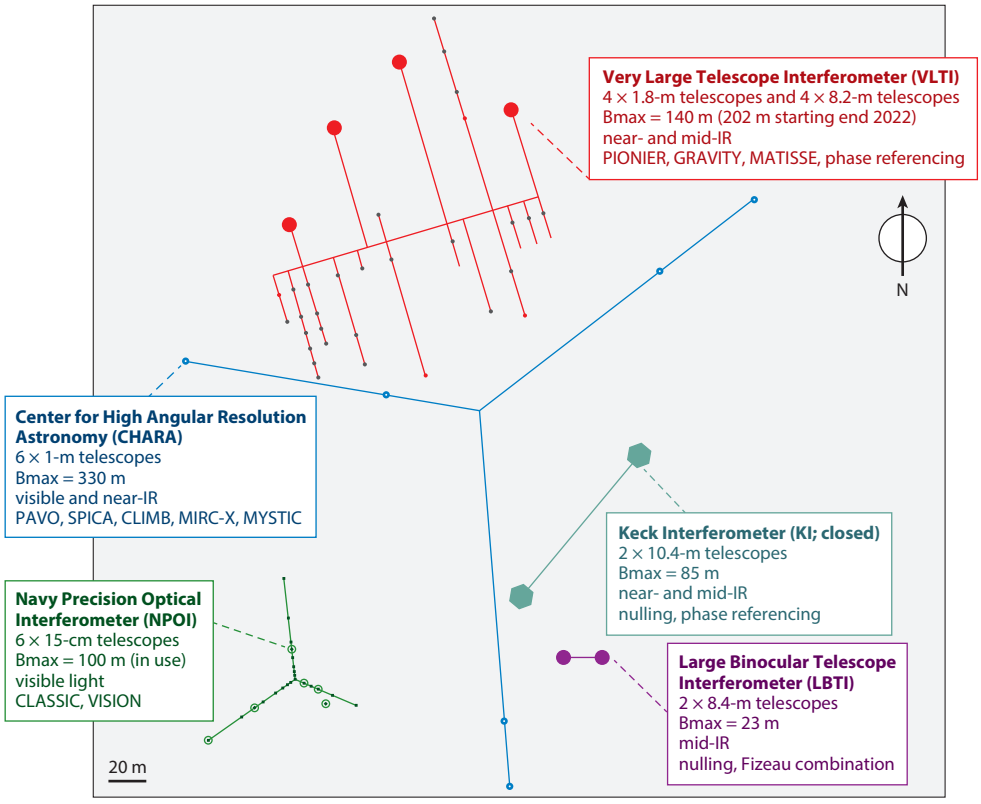

Figure 1

This sketch shows the footprints of modern O/IR interferometers, with telescopes and baselines to scale. The telescopes for KI (*teal*), LBTI (*purple*), CHARA (*blue*), and VLTI-UTs (*red large circles*) are fixed, whereas the NPOI (*green*) and VLTI-ATs (*red small circles*) telescopes are mobile and can be repositioned. Abbreviations: AT, Auxiliary Telescope; CHARA, Center for High Angular Resolution Astronomy array; KI, Keck Interferometer; LBTI, Large Binocular Telescope Interferometer; NPOI, Navy Precision Optical Interferometer; O/IR, optical/infrared; UT, Unit Telescope; VLTI; Very Large Telescope Interferometer.

and orientation on sky. The source brightness distribution is then given by the Fourier transform. Each radio telescope is diffraction limited, with a flat wave front across its aperture. With low-noise, phase-sensitive radio amplifiers, all baselines can be measured simultaneously with little loss of signal or extra noise even for many telescopes. Because early radio interferometry operated at long wavelengths and narrow bandwidths, the coherence length is large, and the interference is not perturbed much by the Earth atmosphere. As a result, the fringe can be maintained fairly easily over a long time and over a wide field of view.

The situation in the O/IR is very different. Because of the short wavelengths, the product of coherence length and coherence time is $\approx 10^{6-8}$ smaller than for radio wavelengths. Other than for radio wavelengths, there are no low-noise heterodyne mixers and amplifiers for the O/IR wavelengths, such that for multiple aperture interferometry the beams have to be split multiple times, resulting in large light losses. On the positive side, flux densities for thermal sources—like stars—are substantially larger for O/IR wavelengths; however, this advantage is eaten up by the need for multimirror, free beam propagation with much lower throughput. Taken together, it is clear that O/IR interferometry is orders of magnitude more challenging than radio interferometry.

Coherence time, τ_0: time span for which the root-mean-square phase fluctuations from the atmosphere are 1 rad

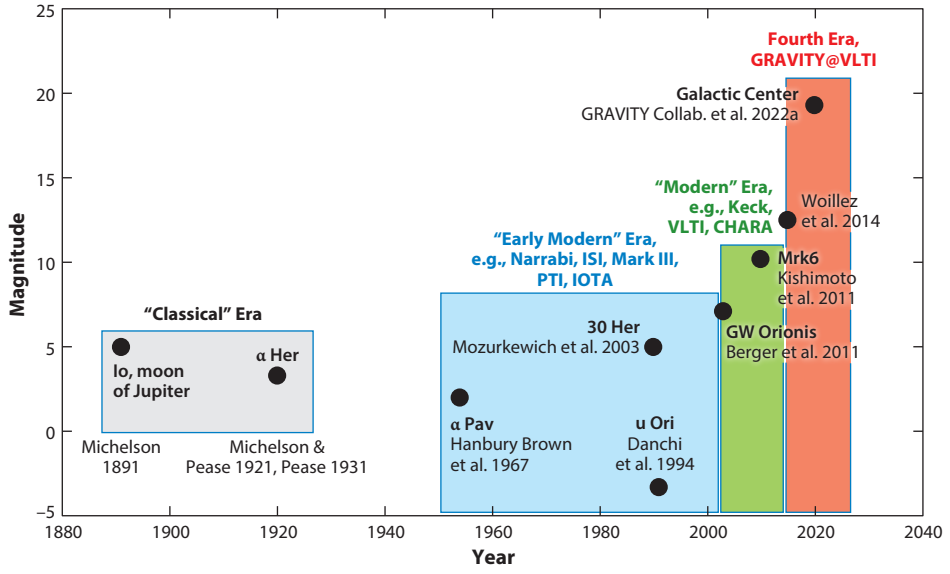

Figure 2

Sensitivity of O/IR interferometry from the "classical" era with visual "by eye" measurements, followed by the "Early Modern" and "Modern" eras, to the latest advances from the fourth era with dual-beam phase referencing. After a century of moderate improvement, the past decade has seen an increase by several orders of magnitudes. Abbreviation: O/IR, optical/infrared.

This is especially the case when aiming for long exposures, which require finding at least one bright- and close-enough object to stabilize the fringes. Although this is the case all over the sky for radio interferometers, we are very far from this situation in the optical because of atmospheric turbulence. But we are currently witnessing this transition for IR wavelengths with performance increases by large factors.

Adaptive optics (AO): technique to correct for atmospheric turbulence and recover diffraction-limited resolution of telescopes, using either a natural or a laser guide star

Integrated optics (IO): optical equivalent to electronic integrated circuits (ICs); dielectric chips implanted with optical waveguides providing beam splitters, combiners, delay lines, nulling, and more

1.3. Performance Increase by Large Factors

We suggest a fourth era of O/IR interferometry has begun with GRAVITY and the advent and routine use of dual-beam phase referencing on 8-m-class telescopes (**Figure 2**). The combination of adaptive optics (AO), dual-beam interferometry, and the ability to track the fast atmospheric fluctuations on a bright nearby star has allowed a breakthrough in sensitivity, extending coherent integrations from 50 ms to >50 s, which is a 1,000-fold jump. Although the first demonstration was the early ASTRA (Astrometric and Phase-Referenced Astronomy) experiment on the Keck Interferometer, the VLTI/GRAVITY project, initiated in 2005 by later Nobel Laureate Reinhard Genzel, has mastered the technique and, together with new detectors, integrated optics (IO) and improved laser metrology, allowing breakthroughs on the Galactic Center, exoplanets, and active galactic nuclei (AGNs).

1.4. Introduction: Summary Points

1. O/IR interferometry has matured and is offered at four major facilities.
2. VLTI and LBTI possess 8-m-class telescopes for high sensitivity; CHARA and NPOI provide higher angular resolution and focus on imaging.
3. A new era of dual-beam phase-referenced interferometry has begun, allowing fringe detection on objects fainter than 19 mag with VLTI/GRAVITY.

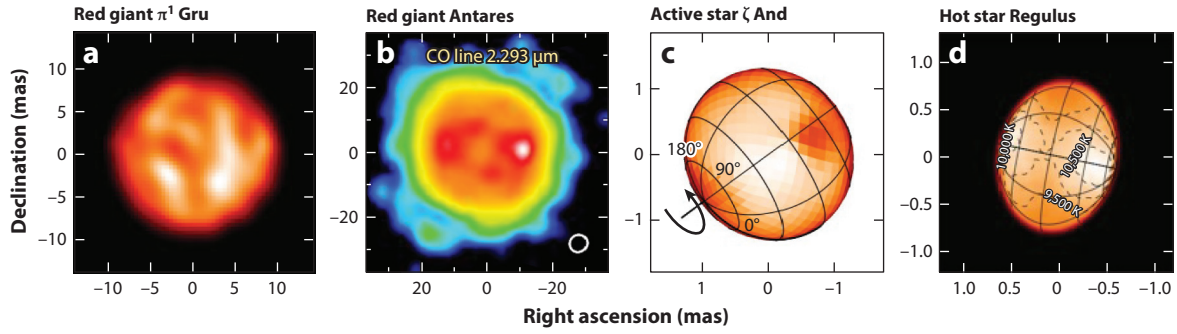

Figure 3

The past decade has seen a breakthrough in stellar imaging as 4- and 6-telescope interferometers now have sufficient UV coverage and angular resolution to resolve the surfaces of red giants and supergiants, magnetically active stars, and even the closest hot rapid rotators. Panel *a* adapted with permission from Paladini et al. (2018); copyright 2018 Springer Nature. Panel *b* adapted with permission from Ohnaka et al. (2017); copyright 2017 Springer Nature. Panel *c* adapted with permission from Roettenbacher et al. (2016); copyright 2016 Springer Nature. Panel *d* adapted with permission from Che et al. (2011); copyright 2011 AAS.

2. ASTROPHYSICAL BREAKTHROUGHS

2.1. Imaging of Stellar Surfaces

The current 4- and 6-telescope arrays have made interferometric imaging routine. Simple objects like binary stars have been imaged for some time but rarely offered advantages over model fitting. More challenging and scientifically fruitful is imaging of stellar surfaces, in which complex phenomena, such as convection and magnetic fields, play out and defy simple parameterization.

Evolved stars host a number of nontrivial and interesting kinds of stellar physics—pulsations, dust production, convective spots—and these change on monthly to yearly timescales. Early imaging efforts (e.g., IOTA; Haubois et al. 2009) suffered from sparse UV coverage due to the small number of telescopes and limited baselines available. More recently, efforts at the VLTI Auxiliary Telescopes (ATs) and CHARA have led to remarkable images of red giants (**Figure 3**). They include state-of-the-art images by Paladini et al. (2018), with approximately eight pixels across the photosphere, and rigorous interpretations inferred through 3D numerical simulations (e.g., Chiavassa et al. 2009). With high spectral resolution, it is now possible to go beyond diameters and imaging of molecular shells (e.g., Perrin et al. 2004, 2020; Le Bouquin et al. 2009) and even kinematically resolve motions within molecular shells using, e.g., CO bandhead transitions (Ohnaka et al. 2017).

The long baselines of CHARA open up imaging for stars too far away or too small for other arrays. Sunspots caused by stifled convection from strong localized magnetic fields are seen on the Sun and inferred on other stars from photometric variations. Roettenbacher et al. (2016) and Parks et al. (2021) published images of huge magnetic spots on all sides of the ζ Andromedae and λ Andromedae systems, respectively, finding asymmetric distributions of spots quite unlike the Sun's.

Lastly, submilliarcsecond angular resolutions also allow imaging the bloated surfaces of the brightest, rapidly rotating, hot stars (e.g., van Belle 2012), e.g., the surface of the B-star Regulus with a highly oblate surface distorted by centrifugal forces and strong equatorial "gravity" darkening (Che et al. 2011). Results on a half-dozen hot stars have led to new insights into nonspherical energy transport and advanced first-principle modeling of rotating stars (e.g., Espinosa Lara & Rieutord 2013).

2.2. Revealing the Inner Astronomical Units of Circumstellar Disks

Young stellar objects (YSOs): newly formed stars generally still surrounded by planet-forming disks; examples include T Tauri stars ($M < 1.5\,M_\odot$) and Herbig Ae/Be stars ($M > 1.5\,M_\odot$)

Closure phase: interferometric observable immune to atmospheric turbulence, made from the sum of three fringe phases measured around a closed triangle of baselines

One of the most fast-developing and exciting areas of astronomy today is planet formation. The milliarcsecond angular resolution of O/IR interferometers translates into about 0.1 AU physical scale at nearby star-forming regions, revealing the signposts of planet formation, orbiting and outflowing dust, and complex physics of the star–disk connection that generates jets and outflows and transports angular momentum to the forming star (see, e.g., Dullemond & Monnier 2010, for an overview). IR interferometry combined with Atacama Large Millimeter/submillimeter Array (ALMA)'s view of the outer disk (e.g., Andrews et al. 2018) and O/IR coronagraphy of scattered light (e.g., Benisty et al. 2022) is providing a rich and comprehensive picture of how planets are assembling in the earliest stages of their formation.

The advent of sensitive 4-telescope combiners at VLTI have revolutionized studies of young stellar objects (YSOs) by vastly increasing the number of objects that are observable, expanding wavelength coverage, improving homogeneity of the samples, and probing asymmetries using closure phases. Lazareff et al. (2017) and GRAVITY Collab. et al. (2019c) measured homogeneous sizes and orientations of dozens of Herbig Ae/Be stars in *H* and *K* bands, vastly improving the data quality over earlier pioneering studies (e.g., Monnier & Millan-Gabet 2002). The size–luminosity diagram (**Figure 4**) shows a robust correlation over many orders of magnitude in luminosity, though with large scatter, potentially due to stochasticity from the formation of young planets. Kluska et al. (2020a) used advanced image reconstruction algorithms for some of these targets (HD 45677 in **Figure 4**), finding only a few ring-like structures, with more often centrally bright emission. Recent multiepoch studies have further found a strong time variability in some objects (Kobus et al. 2020, GRAVITY Collab. et al. 2021f), the cause of which is unclear. A large sample

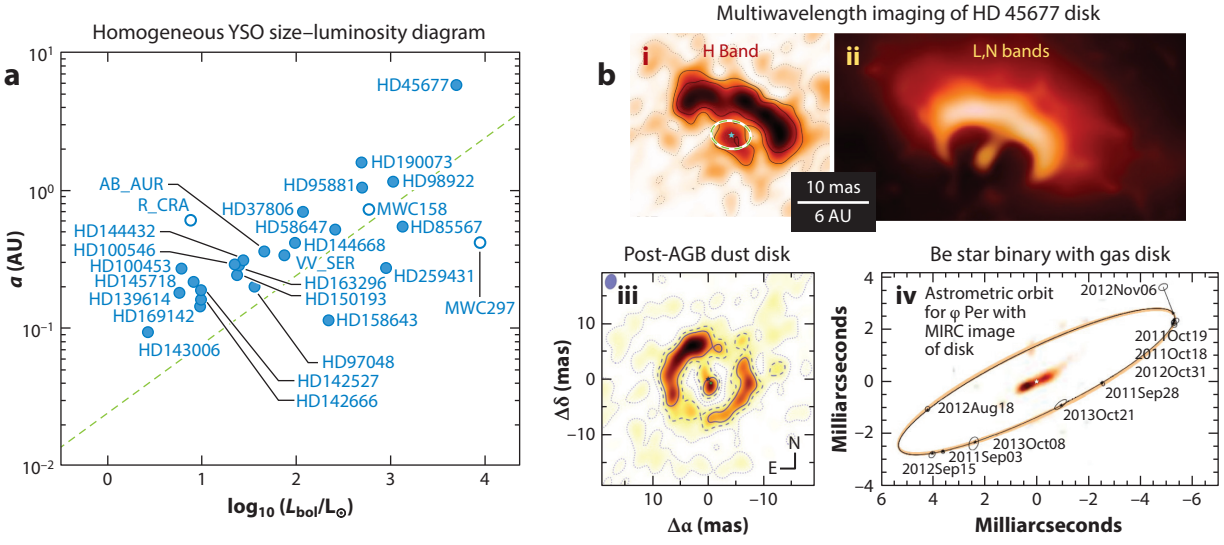

Figure 4

IR interferometers now probe statistically significant, homogeneous samples of YSOs, for example, to study their size–luminosity relations (*a*). Furthermore, it is the only current technology that can image the inner ~1 AU of planet-forming disks, Be star gas disks, interacting binaries, and circumbinary disks. Panel *a* adapted with permission from Lazareff et al. (2017); copyright 2017 ESO. Panel *b*, subpanel *i*, adapted with permission from Kluska et al. (2020a); copyright 2020 ESO. Panel *b*, subpanel *ii*, adapted with permission from Lopez et al. (2022); copyright 2022 ESO. Panel *b*, subpanel *iii*, adapted with permission from Hillen et al. (2016); copyright 2016 ESO. Panel *b*, subpanel *iv*, adapted with permission from Mourard et al. (2015); copyright 2015 ESO. Abbreviations: AGB, asymptotic giant branch; MIRC, Michigan InfraRed Combiner; YSO, young stellar object.

of T Tauri disks in the *K* band (GRAVITY Collab. et al. 2021e) also found a strong breakdown of the size–luminosity relation (in line with earlier Keck Interferometer results; Akeson et al. 2005), indicating that scattering and accretion are of greater importance.

The Keck Interferometer and VLTI have also allowed researchers to spatially and spectrally resolve the hydrogen Brγ line, probing the kinematics of accretion and the star–disk connection on sub-astronomical-unit scales. Early studies did not find a clear picture: some disks showed compact Brγ emissions smaller than the dust ring, whereas others showed emission on the same scales (Kraus et al. 2008, Eisner et al. 2009). Although only a few results have been obtained so far (e.g., Bouvier et al. 2020), GRAVITY has the potential to carry out a large survey of Brγ line emission as well as the CO bandhead (e.g., GRAVITY Collab. et al. 2020d, 2023). The Visible spEctroGraph and polArimeter (VEGA) on CHARA (Perraut et al. 2016) was first to resolve the Hα line in the accretion disk of AB Aur, finding a larger-than-expected extent from the magnetocentrifugal wind launched between the star and the dusty disk's inner edge.

Sagittarius A* (SgrA*): name of the radio source at the Galactic Center containing a supermassive black hole

The shape of the dust sublimation front and contribution of gas/dust emissions very close to the star are too small to be definitively resolved by VLTI. CHARA, with >300-m baselines, has fully resolved the inner disk emission for two bright Herbig Ae/Be stars and found strong emission coming from inside the putative dust evaporation front (Setterholm et al. 2018), corroborating earlier studies (e.g., Benisty et al. 2010). Recently, VLTI and CHARA data have been combined to directly image the rim shape for the Herbig Be star v1295 Aql (Ibrahim et al. 2023), finding a bright thin ring but with mysterious inner emission.

New IR interferometry has validated some untested theory and solved long-standing mysteries. Labdon et al. (2021) found the disk temperature profile of the prototype FU Ori object to closely match $T \propto r^{-\frac{3}{4}}$, a 30-year-old prediction by Hartmann & Kenyon (1985). The Brγ emission around TW Hya was interpreted as definitive proof of the magnetospheric accretion paradigm (GRAVITY Collab. et al. 2020f). The complex dust geometry for the young interacting system GW Ori was finally solved by Kraus et al. (2020a). Lastly, Labdon et al. (2019) and Bohn et al. (2022) combined IR interferometry with AO to prove that inner disk misalignments produce the dark shadow bands seen at 100-AU scales for many disks.

Disks and outflows have also been imaged around other kinds of stars. Mourard et al. (2015) were able to image the ϕ Per disk with CHARA in both Brα and continuum (**Figure 4**), showing a clear connection between the disk geometry and the close-in binary companion. Circumstellar disks can also form in close interacting binaries (Zhao et al. 2008) and in post-AGB systems (**Figure 4**; Hillen et al. 2016). The recent commissioning of the MIR combiner VLTI/MATISSE (Multi AperTure mid-Infrared SpectroScopic Experiment; see the early result by Lopez et al. 2022, in **Figure 4**) will revolutionize studies of dusty outflows in a wide variety of environments including AGB stars (e.g., Chiavassa et al. 2022).

2.3. Testing the Black Hole Paradigm in the Galactic Center

Motivated by the discovery of the first quasars in the 1960s, Lynden-Bell & Rees (1971) proposed that most galactic nuclei, including the Galactic Center, might host a supermassive black hole (SMBH). The discovery of the compact radio source Sagittarius A* (SgrA*) (Balick & Brown 1974) at the core of the central nuclear star cluster provided some evidence for their proposition. However, SgrA* is faint in all bands other than the radio and submillimeter. With abundant gas in the inner 1 pc to fuel a potential SMBH, the case for an extremely underluminous SMBH was considered fairly unconvincing. This only changed with the advent of near-IR (NIR) Speckle and AO images of the central 1 pc. Proper motions and later full orbits of stars demonstrated the existence of a compact central mass. The combination of precision astrometry better than 1 mas

2020 NOBEL PRIZE IN PHYSICS FOR THE DISCOVERY OF THE GALACTIC CENTER BLACK HOLE

The Nobel Prize in Physics 2020 was awarded to Reinhard Genzel and Andrea Ghez for the "discovery of a supermassive compact object at the center of our galaxy" and to Roger Penrose "for the discovery that black hole formation is a robust prediction of the general theory of relativity." The discovery of the Galactic Center black hole is building on the experimental breakthroughs in high angular resolution astronomy over the past 30 years, starting from speckle interferometry to recover the diffraction-limited resolution of large telescopes in the 1990s, followed by AO and imaging spectroscopy in the 2000s. In 2005, Reinhard Genzel initiated the long baseline interferometer GRAVITY, providing milliarcsecond resolution imaging and a few tens of microarcsecond astrometry—the topic of this article.

with spectroscopy allowed for weighing the enclosed mass, measuring its distance, and setting tight constraints on the density and therefore on the nature of the enclosed mass. By the end of the 2000s, the analysis of several dozen orbits in combination with radio measurements of the size and motion of SgrA* established that the radio source must be a massive black hole with about $4 \times 10^6\,M_\odot$, "beyond any reasonable doubt" (for a review, see Genzel et al. 2010). (See the sidebar titled 2020 Nobel Prize in Physics for the Discovery of the Galactic Center Black Hole.)

The dynamical measurements from AO images allowed the derivation of the mass of the central object with a few percent accuracy. The motion of the stars follow almost perfect Keplerian orbits, even for stars like S2 that passes the central source as close as $1{,}400\,R_S \approx 120$ AU (Schwarzschild radius: $R_S = 2GM/c^2$). Following the pericenter passage of S2 in 2002, it became clear that the first-order general relativity (GR) effects will come in reach with precision observations (Rubilar & Eckart 2001). Despite the fact that a black hole is a genuine prediction of GR, the signatures of GR on the stellar orbits with the leading post-Newtonian terms ($O(\beta^2)$, $\beta = v/c$), namely gravitational redshift and Schwarzschild precession, are small perturbations w.r.t. the Keplerian motion (for a review, see Alexander 2005). The gravitational redshift scales with $\beta^2 \approx R_S/R$. In case of S2, the effect is approximately $200\,\mathrm{km\,s^{-1}}$ compared to the maximum velocity of $7{,}700\,\mathrm{km\,s^{-1}}$ at pericenter passage. The Schwarzschild precession rotates the elliptical orbit by ≈12.1 arcmin per 16 years revolution. In order to measure the effects, a significant improvement (by a factor of 4–10) in astrometry compared to what was possible in 2010 was needed. This posed one of the main science drivers for the development of the GRAVITY instrument (Eisenhauer et al. 2008, Paumard et al. 2008). Since its first light (GRAVITY Collab. et al. 2017a), GRAVITY has been regularly observing the central S-stars and SgrA*. On May 19, 2018, S2 passed pericenter with 2.6% of the speed of light. By simultaneously monitoring the star's radial velocity and motion on the sky, GRAVITY Collab. et al. (2018a) were able to detect the gravitational redshift and transverse Doppler effect at high significance (later confirmed by Do et al. 2019). The statistical robustness of the redshift detection was further improved by GRAVITY Collab. et al. (2019a) to more than 20σ significance. Amorim et al. (2019) used two atomic transition lines in the spectrum of S2 to test one pillar of the Einstein equivalence principle and, thus, GR and the local position invariance (LPI). By separately measuring the redshift of the hydrogen and helium lines in the stellar spectrum, effectively two independent clocks can be probed, while moving through the black hole's gravitational potential. The results set an upper limit on a violation of the LPI of 5×10^{-2} for a change of potential that is six magnitudes larger than accessible with terrestrial experiments.

Black hole: object so massive and compact that not even light can escape, as described by Einstein's General Theory of Relativity

Only a few months after the pericenter passage of S2, GRAVITY captured several bright flares showing circular motion of the emission region (**Figure 5**; GRAVITY Collab. et al. 2018b). The observed motion shows an orbit of a compact polarized hot spot of IR synchrotron emission at approximately 3 to 5 Schwarzschild radii of a black hole of 4.3 million solar masses. This corresponds to the region just outside the innermost, stable, prograde circular orbit (ISCO) of a Schwarzschild–Kerr black hole. The simultaneous motion, light curve, and polarization measurements of the flares allowed researchers to constrain the inclination of the flaring region to a near face-on ($i \approx 30$ deg) orbit. The results are in remarkable agreement with the inclination and size later derived for the radio image of SgrA* (Event Horizon Telesc. Collab. et al. 2022), suggesting that both IR and radio emission originate from the same region. The flare detection and the Event Horizon Telescope (EHT) image provide unique evidence that 4.3 million solar masses are contained in a region of a few R_S (**Figure 5*c***, subpanel *i*), which is a mass density only explained by a black hole. GRAVITY Collab. et al. (2020a) substantiated that SgrA* has two states: The bulk of the IR emission is generated in a lognormal process with a median flux density of 1.1 mJy. This quiescent emission is supplemented by sporadic bright flares, which create the observed power-law extension of the flux distribution and are also observed in X-rays.

Two years after the detection of the gravitational redshift, GRAVITY Collab. et al. (2020b) reported the detection of the prograde Schwarzschild precession induced by the gravitational field of the SMBH (**Figure 5**). The authors measured the mass of the black hole with 0.4% accuracy and ruled out the presence of a binary SMBH. GRAVITY Collab. et al. (2022b) refined the measurement and set an upper limit on an extended mass, e.g., a putative cusp of stellar remnants surrounding the SBMH, of less than $3{,}000\,M_\odot$ within the apocenter of S2. The monitoring of the S stars not only allowed testing of the black hole paradigm but also tackling of a classical astrophysical problem: the distance of the Sun from the Galactic Center. GRAVITY determined the distance between the Sun and the SMBH to $R_0 = 8{,}277$ pc with 0.4% accuracy (GRAVITY Collab. et al. 2019a, 2020b, 2021b), confirming that the SMBH is located at the center of the Milky Way Bulge ($R_{0,\mathrm{bulge}} = 8{,}210 \pm 80$ pc, Bland-Hawthorn & Gerhard 2016).

GRAVITY has delivered precision tests of Einstein's general theory of relativity and the so-far-strongest experimental evidence that the compact mass in the Galactic Center (SgrA*) is indeed a Schwarzschild–Kerr black hole. What can we expect in the future? The upgrade of GRAVITY, with its current sensitivity limit of $m_K \approx 19.5$ (GRAVITY Collab. et al. 2021a), to GRAVITY+ (Eisenhauer 2019, GRAVITY Collab. et al. 2022c) will push the sensitivity limit to $m_K > 22$, with the expectation of revealing more stars on even smaller orbits than that of S2. The astrometry from interferometry and the radial velocities from upcoming 30–40-m telescopes will then allow probing of higher-order GR effects such as frame dragging of space-time due to the spin of the black hole or the imprint of the black hole's quadrupole moment, and thereby might even provide a test of the general relativistic no-hair theorem.

2.4. Resolving the Broad-Line Region and Imaging the Hot Dust in Active Galactic Nuclei

An AGN is a massive accreting black hole in the center of a galaxy with an Eddington ratio $L_{\mathrm{AGN}}/L_{\mathrm{Edd}} > 10^{-5}$, where L_{AGN} is the bolometric luminosity and L_{Edd} is the Eddington luminosity (e.g., Netzer 2015). AGNs are thought to play an important role in galaxy evolution: Energy released by AGNs through radiation or powering outflows (i.e., AGN feedback) can transform star-forming galaxies into quiescent galaxies. The unified model of AGNs assumes that a dust torus obscures the central engine, accretion disc, and the broad-line region (BLR), such that the AGN can only be observed directly from polar directions (Antonucci & Miller 1985).

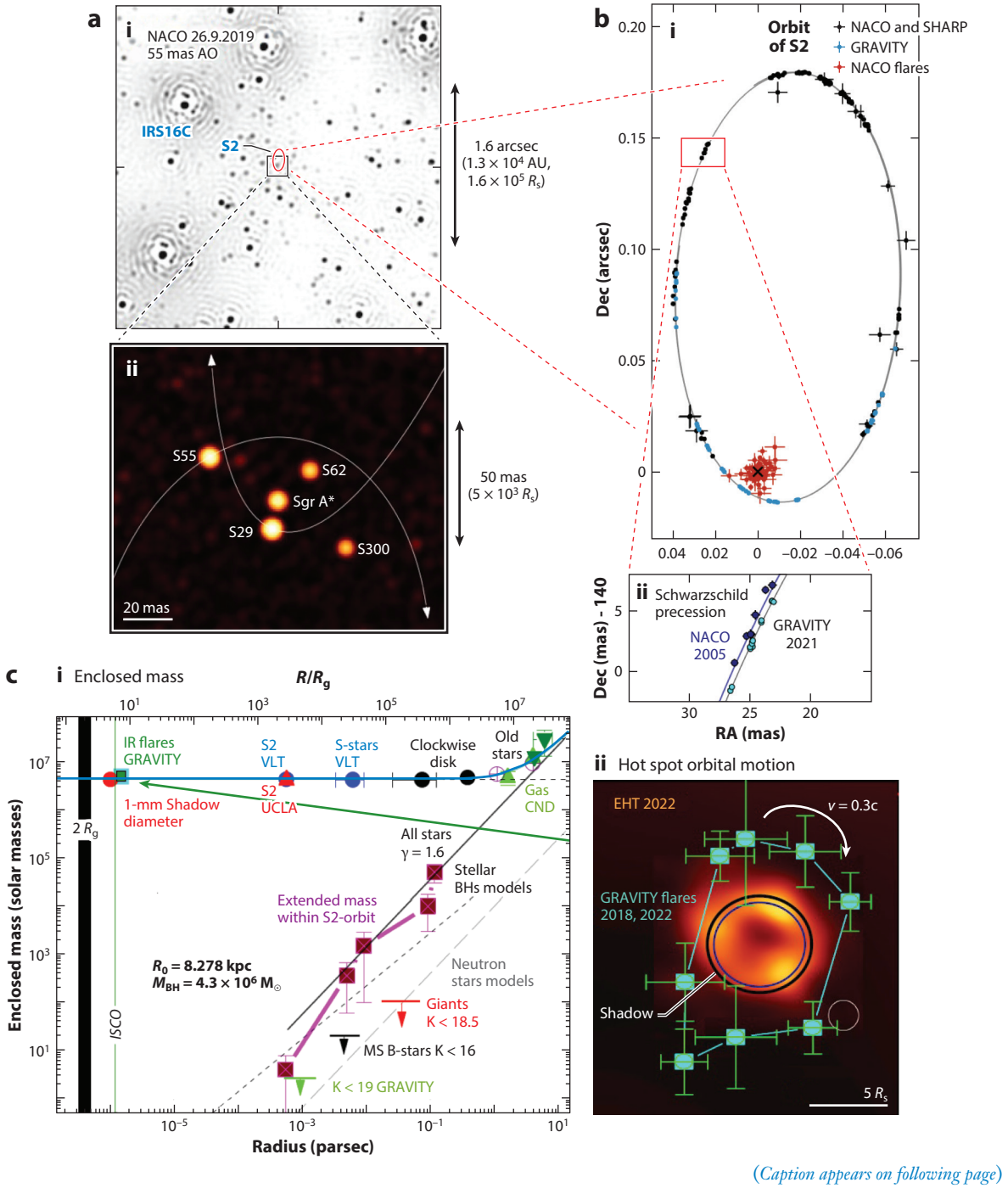

(*Caption appears on following page*)

Figure 5 (*Figure appears on preceding page*)

(*a*, *i*) AO image of the Galactic Center obtained with an 8-m telescope. (*a*, *ii*) Interferometric image of the central 0.1 arcsec. The crowded region cannot be resolved with single-telescope observations. (*b*, *i*) S2-SgrA* orbit. (*b*, *ii*) Zoom-in of the orbit of S2. The orbit does not close due to the Schwarzschild precession. (*c*, *i*) Enclosed mass of the central 1 pc centered on SgrA*. (*c*, *ii*) IR flare positions observed over approximately 30 min. The motion shows an ($i \sim 30$ deg) orbit of a hot spot at 3–4 R_S (GRAVITY Collab. et al. 2018b). The background shows the EHT image of SgrA*. Panel *a* adapted with permission from GRAVITY Collab. et al. (2022a); copyright 2022 ESO. Panel *b* adapted with permission from GRAVITY Collab. et al. (2020b; copyright 2020 ESO) and GRAVITY Collab. et al. (2022b; copyright 2022 ESO). Panel *c*, subpanel *ii*, (background) adapted with permission from Event Horizon Telesc. Collab. et al. (2022); copyright 2022 AAS. Abbreviations: AO, adaptive optics; BH, black hole; CND, circumnuclear disk; EHT, Event Horizon Telescope; MS, main sequence; RA, right ascension; VLT, Very Large Telescope.

IR interferometry has played a crucial role in the study of the torus region because the apparent size of 1 pc at the distance of the closest AGNs (~20 Mpc) is <10 mas, a scale that can only be resolved with long-baseline interferometry. Although AGNs are intrinsically bright in the IR, their relatively large distances require 8-m telescopes for observations. Early papers, using single-baseline interferometers and V^2-fitting, identified the presence of multiple dust components with an elongated (1.4 × 0.5 pc) 600–800 K dust core (e.g., Jaffe et al. 2004). About two dozen AGNs have been partially resolved with the Keck interferometer (e.g., Swain et al. 2003, Kishimoto et al. 2011), early VLTI (e.g., Burtscher et al. 2013), and more recently GRAVITY (GRAVITY Collab. et al. 2020e, Leftley et al. 2021). This led to a dust size–luminosity relation for nearby AGNs, independent of the relation inferred from dust reverberation mapping (**Figure 6*d***).

The advent of the second-generation VLTI instruments and the combination of four 8-m telescopes allowed, for the first time, reconstruction of images of the hot dust in AGN. GRAVITY Collab. et al. (2020h) resolved the central 2 pc of NGC 1068 in the *K* band with a spatial resolution of 3 mas (**Figure 6*a***) and found a ring-like structure on subparsec scales. The size matches that expected for the dust sublimation region, and the apparent orientation is similar to that of the maser disc, arguing for a common origin. This scenario is at odds with a geometrically and optically thick clumpy torus and instead argues for the presence of a dusty thin disc around the AGN, which is screened by dense and turbulent gas distributed on scales of 1–10 pc, e.g., from AGN-driven outflows. This interpretation has been contested by Gámez Rosas et al. (2022), who resolved the central region using MATISSE at lower resolution but longer wavelengths from 3.7 to 12 μm (**Figure 6*b***). The derived dust temperatures and absorption values are consistent with a thick, nearly edge-on disk as predicted by the torus model. The different interpretation is largely driven by the assumptions made to align the radio continuum and maser emission and IR image.

The BLR with an angular size <0.1 mas is even smaller than the hot dust region, and it is impossible to image even with the VLTI. Instead, the kinematics can be studied by spectro-astrometry, which measures the photocenter shift of the atomic gas as a function of wavelength (or velocity) across the emission line. The photocenter shift results in a small differential phase signal of <1 deg, whose detection requires high sensitivity and deep integrations. GRAVITY Collab. et al. (2018c) for the first time detected the characteristic S-shaped phase signal of a rotating disk in the broad Paα emission line of the quasar 3C 273 (**Figure 6*c***). The signal is well described by a model (following Pancoast et al. 2014) of fast moving gas clouds in a thick disk in Keplerian rotation around a SMBH of 1.5–4.1 $\times 10^8$ $M_\odot$. The inclination and position angles agree with those inferred for the radio jet. The measured emission radius is $R_{BLR} = 0.12 \pm 0.03$ pc (at an angular diameter distance of 548 Mpc). To this day, three BLRs have been resolved successfully with spectroastrometry (3C 273, NGC 3783, and IRAS 09149-6206; GRAVITY Collab. et al. 2018c, 2020c, 2021c) (**Figure 6**), which revealed their structure, kinematics, and angular BLR sizes with an unrivaled spatial resolution. The joint analysis of the angular BLR size measurement from GRAVITY and the linear BLR size from reverberation mapping campaigns allowed Wang et al. (2020) to

Spectroastrometry: a measurement of an object's photocenter across a spectral line that allows microarcsecond differential precision

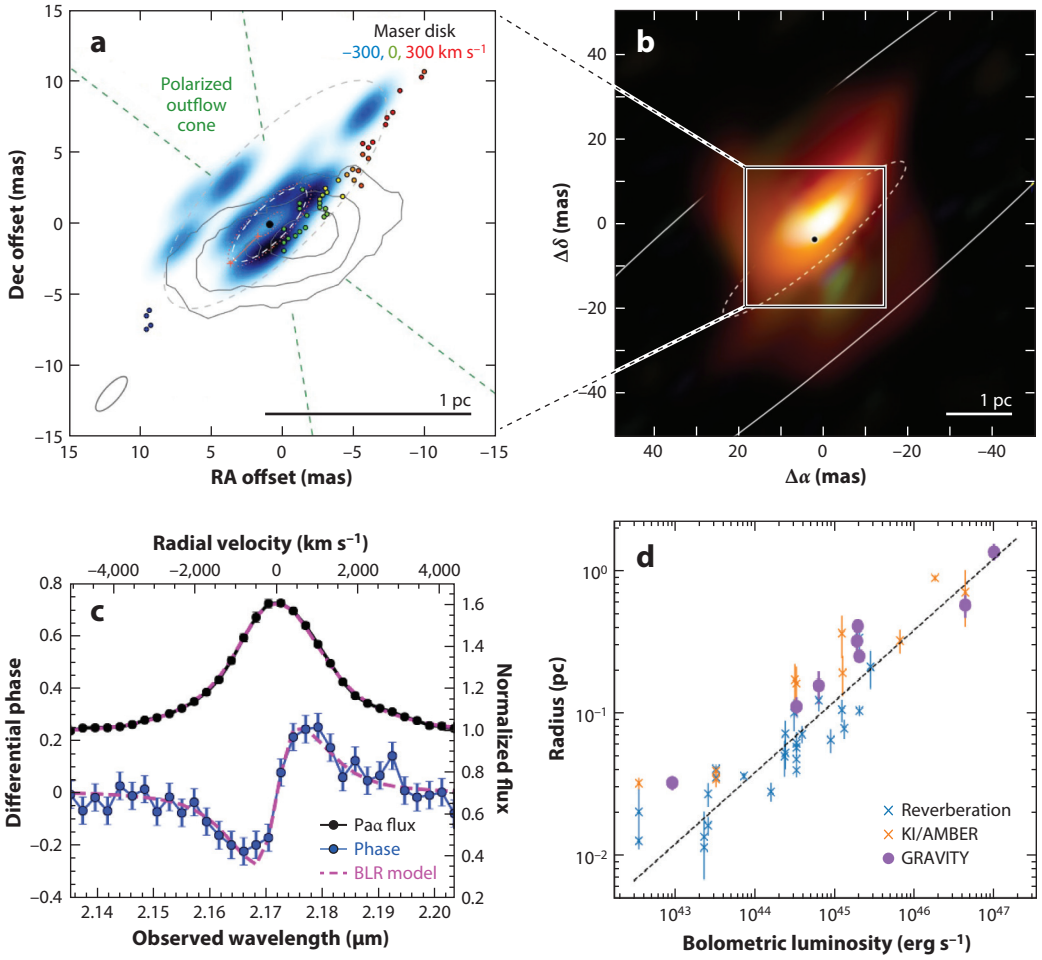

Figure 6

(*a*) *K*-band image of the inner 2 pc of NGC 1068. The dashed white ellipse corresponds to the dust sublimation radius. The filled black circle indicates the AGN, and colored circles represent the kinematic centers of the masers. (*b*) MATISSE multicolor image of NGC 1068. (*c*) GRAVITY Collab. et al. spatially resolved the broad emission line kinematics of 3C 273. Paα line profile (*black*) showing nonzero phases and a change of sign across the broad emission line. (*d*) Radius–luminosity relation for dust-size measurements (*blue* and *orange crosses* from literature; *filled circles*, GRAVITY Collab. et al. 2020e). The dashed line is the $R \sim L^{1/2}$ fit to reverberation measurements (Koshida et al. 2014). Panel *a* adapted with permission from GRAVITY Collab. et al. (2020h); copyright 2020 ESO. Panel *b* provided by of ESO/Walter Jaffe, Gámez Rosas et al. (2022); copyright 2022 Springer Nature. Panel *c* adapted with permission from GRAVITY Collab. et al. (2018c); copyright 2018 Springer Nature. Panel *d* adapted with permission from GRAVITY Collab. et al. (2020e); copyright 2020 ESO. Abbreviations: AGN, active galactic nucleus; AMBER, Astronomical Multi-BEam combineR; BLR, broad-line region; KI, Keck Interferometer; MATISSE, Multi AperTure mid-Infrared SpectroScopic Experiment.

derive an angular distance of 3C273 of 552^{+97}_{-79} Mpc and an independent measurement of the Hubble constant $H_0 = 72\,\mathrm{km\,s^{-1}\,Mpc^{-1}}$ with 15% uncertainty. In a similar way, GRAVITY Collab. et al. (2021d) found a geometric distance to NGC 3783 of 39.9^{+15}_{-12} Mpc and derived H_0 with a 30% uncertainty. GRAVITY already demonstrated first fringes of a redshift $z = 2.5$ quasar (GRAVITY Collab. et al. 2022c). Future BLR observations of a reasonably sized sample (≈30 AGNs) will provide a new tool for measuring the masses of black holes at cosmological distances and might

allow for testing of the H_0 tension with $\ll$3% accuracy (Wang et al. 2020). A similar tool might be provided by the interferometric dust parallax measurement as introduced by Hönig et al. (2014).

2.5. Observations of Exoplanets and Spectroscopy of Their Atmosphere

Although only applicable for a few dozen exoplanets so far, direct imaging offers the unique possibility of probing the thermal emission from the exoplanet's atmosphere, which is key for measuring the composition of their dense atmospheres. However, direct imaging is impaired by the small separation and the contrast between the exoplanets and their host stars, and only young, hot ($\lesssim$1,000 K), and far ($\gtrsim$10 AU) planets are observable by AO and coronagraphy. IR interferometry has pushed both limits by orders of magnitude, providing the so far best-quality, high-resolution spectra from hot planets, orbit measurements with a few tens of microarcsecond astrometry, and first direct observations of planets previously known only from radial velocities.

The first detection of an exoplanet with interferometry (GRAVITY Collab. et al. 2019b) was HR 8799e, a planet only 0.39 arcsec from its host star. The spectra from GRAVITY are roughly ten times higher in signal-to-noise ratio (SNR) than possible with single-telescope observations. This allows retrieving the properties of clouds and disequilibrium chemistry in the exoplanet atmosphere (Mollière et al. 2020) and calibrating the mass–luminosity relations for protoplanets. Since this breakthrough, a series of observations have led to spectra for, e.g., β Pic b,c (GRAVITY Collab. et al. 2020g, Lagrange et al. 2020, Nowak et al. 2020) and the PDS 70 protoplanets (Wang et al. 2021). The spectrum from β Pic b (**Figure 7**) allowed researchers to peer into the formation history of this exoplanet: The low C/O ratio measured from the exoplanet spectrum, and the high mass of the exoplanet determined from astrometry suggest a formation through core accretion, with strong planetesimal enrichment.

The higher angular resolution and better contrast of interferometry have also led to first direct detections of exoplanets, which were previously known from radial velocity measurements but are too faint and too close to the host star for imaging with AO and coronagraphs. The first of these radial velocity planets detected and characterized with interferometry was β Pic c (Lagrange et al. 2020, Nowak et al. 2020), an 8–9 $M_{Jupiter}$ planet, orbiting at a distance of only 2.7 AU inside the planet β Pic b discussed above. β Pic c is 11 mag fainter—a factor of 25,000—than the host star and was detected at a separation as close as 96 mas. The astrometric errors for the β Pic b,c planetary systems are as small as 20–50 μas. For the first time, this allowed researchers to measure the mass of an exoplanet from its gravitational imprint on the astrometry of another planet (Lacour et al. 2021).

Limitations of the direct detection of radial velocity planets by interferometry are the small field of view and that the radial velocity technique does not provide the inclination of the orbit and, therefore, the direction to look for the planet. The β Pic planetary system is exceptional in this sense because it is seen edge on, both the debris disk as well as the orbit of the outer planet, thereby providing a good prior estimate for the location of the radial velocity planet. The second radial velocity planet directly detected by interferometry was HD 206893c (Hinkley et al. 2023), an $\approx$12 $M_{Jupiter}$ planet at the limit of the brown dwarf regime and maybe one of the rare planets exhibiting deuterium burning in its center. In this case, the detection of the radial velocity planet was guided by GAIA astrometry, which narrowed down the patrol field to be surveyed with the interferometer. Many additional planet detections are expected from GAIA astrometry (Wallace et al. 2021), which will be reachable with interferometry but not with traditional coronagraphic imaging. The GRAVITY+ upgrade (Eisenhauer 2019) is expected to then see emission from >40 gas giant exoplanets in the young comoving groups close to Earth and an additional 30 exoplanets in more distant star-forming regions.

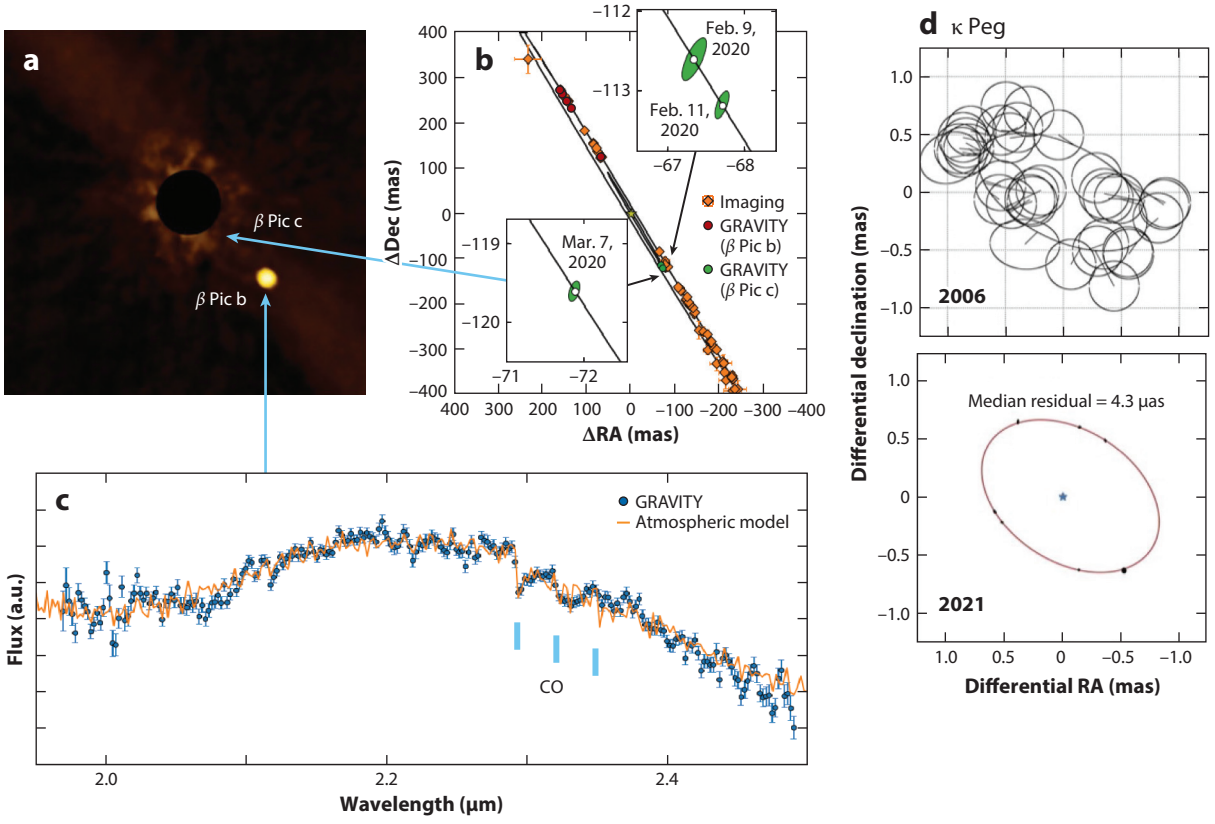

Figure 7

Interferometric observations of exoplanets: (*a*) AO image of the β Pic b exoplanet. (*b*) The superior contrast and angular resolution of GRAVITY allow precision orbital astrometry of β Pic b and β Pic c, the latter being the first exoplanet that was seen by interferometry before conventional AO imaging. (*c*) This spectrum of β Pic b's atmosphere by GRAVITY has a higher signal-to-noise ratio than that from AO and has allowed researchers to measure the C/O ratio, which indicates that the planet has probably formed through core accretion with strong planetesimal enrichment. (*d*) The two orbits shown here illustrate the radical improvement in astrometry of binary stars over the past 15 years. CHARA can now measure the astrometric wobble of κ Peg B about 50× better than the PTI data from 2006. This new astrometric precision should allow discovery of new exoplanets in the next several years. Panel *a* provided by ESO/Anne-Marie Lagrange/SPHERE consortium. Panel *b* adapted with permission from Nowak et al. (2020); copyright 2020 ESO. Panel *c* adapted from GRAVITY Collab. et al. (2020g); copyright 2020 ESO. Panel *d* (*top*) adapted with permission from Muterspaugh et al. (2006); copyright 2006 AAS; panel *d* (*bottom*) adapted with permission from Gardner et al. (2021); copyright 2021 AAS. Abbreviations: AO, adaptive optics; CHARA, Center for High Angular Resolution Astronomy array; PTI, Palomar Testbed Interferometer; RA, right ascension.

Exoplanets have also long been sought using astrometry between two stars (Shao & Colavita 1992). The GRAVITY Collaboration has pursued this route with differential astrometry of young, nearby visual binary systems, e.g., GJ 65 AB, WDS J20452-3120 BC, and HD 142 AB, but results have not been published to date. The PHASES (Palomar High-precision Astrometric Search for Exoplanet Systems) project on the PTI measured differential phase between two close-by stars, achieving ≈100-μas precision (Muterspaugh et al. 2010). This concept was updated for CHARA/MIRC-X (Michigan InfraRed Combiner-eXeter) and VLTI/GRAVITY observations (see **Figure 7**) using precision wavelength calibration and medium spectral dispersion to overlap fringe packets, and demonstrated ≈10–20-μas differential precision sufficient to detect giant exoplanets, though none have been reported so far (Gardner et al. 2022).

2.6. Other Major Advances

There are many other notable firsts from O/IR interferometry in the past decade. Dong et al. (2019), Zang et al. (2020), and Cassan et al. (2022) were able to resolve the multiple images and arcs formed during a microlensing event. Kraus et al. (2020b) used microarcsecond spectroastrometry to measure the rotation axis of an individual star (Kraus et al. 2020b). The high-mass X-ray binaries SS 433 and BP Cru were probed with microarcsecond spectroastrometry to resolve the gas and jet in these systems (GRAVITY Collab. et al. 2017b, Waisberg et al. 2017). Kloppenborg et al. (2010) imaged the transit of a mysterious edge-on dusty disk across the face of the bright star ϵ Aur. Schaefer et al. (2014) watched Nova Del 2013 expand from 0.4 mas on day 2 to >10 mas a month later.

Interferometry is also used to measure fundamental properties of stars, and our current facilities allow for extensive and rigorous surveys of stellar diameters as well as binaries. Here, we highlight the contributions by Boyajian et al. (2012) to calibrate the effective temperature scale for main sequence solar-type stars, Huber et al. (2012) to link precision diameters with asteroseismology using the sensitive visible-light CHARA/PAVO (Precision Astronomical Visible Observations) combiner (Ireland et al. 2008), Sana et al. (2014) to determine binary statistics for massive stars, Gallenne et al. (2015) to measure masses for important distance ladders Cepheids, Montargès et al. (2021) to unveil the cause of Betelgeuse's recent dimming, and Richardson et al. (2021) to measure the first dynamical mass of an N-rich Wolf–Rayet star using a binary separated by only $a = 0.79$ mas.

2.7. Astrophysical Breakthroughs: Summary Points

1. Imaging the surfaces of stars with submilliarcsecond resolution—including evolved stars, magnetic starspots, and rapidly rotating hot stars—is now routine.
2. Warm and hot dust can be imaged around a large number of planet-forming disks and mass-losing stars, revealing unexpected dynamics and complexity.
3. A few tens of microarcsecond astrometry of stars and gas as faint as $m_K = 19$ allowed for testing of GR in the vicinity of the Galactic Center SMBH.
4. NIR and MIR imaging of AGNs allow testing the unified model. Spectroastrometry of BLRs provides a new tool to measure black hole masses and distances.
5. Superior contrast and angular resolution of interferometry produce better exoplanet spectra and orbits than AO coronagraphy.

3. INTERFEROMETRY PRIMER

3.1. Two-Telescope Interferometer, Angular Resolution, and Field of View

Young's two-slit experiment illustrates the basic principles of interferometry (**Figure 8**). When parallel wave fronts from a distant point source go through an aperture with diameter D, the light diffracts over a full-angle $\theta_{\rm beam} = \frac{\lambda}{D}$, where λ is the observing wavelength. This angle is often referred to as the primary beam and typically sets the maximum field of view for most O/IR interferometers. When light goes through another aperture separated from the first by a baseline B, the electric fields interfere and produce a sinusoidal oscillation ("fringe") with a spacing of $\theta_{\rm fringe} = \frac{\lambda}{B}$ (Born & Wolf 1999).

The number of fringes across the pattern is $\frac{B}{D}$, but this is limited when using a broad spectral bandwidth. Then the number of fringes across an interferogram is set by the coherence length $\Lambda = \frac{\lambda^2}{\Delta\lambda}$ and is related to the spectral resolution $R = \frac{\lambda}{\Delta\lambda}$. If R is too small, fringes will not completely fill the diffraction pattern and this further restricts the effective field of view to $\theta \sim \frac{\lambda}{B}R$. The

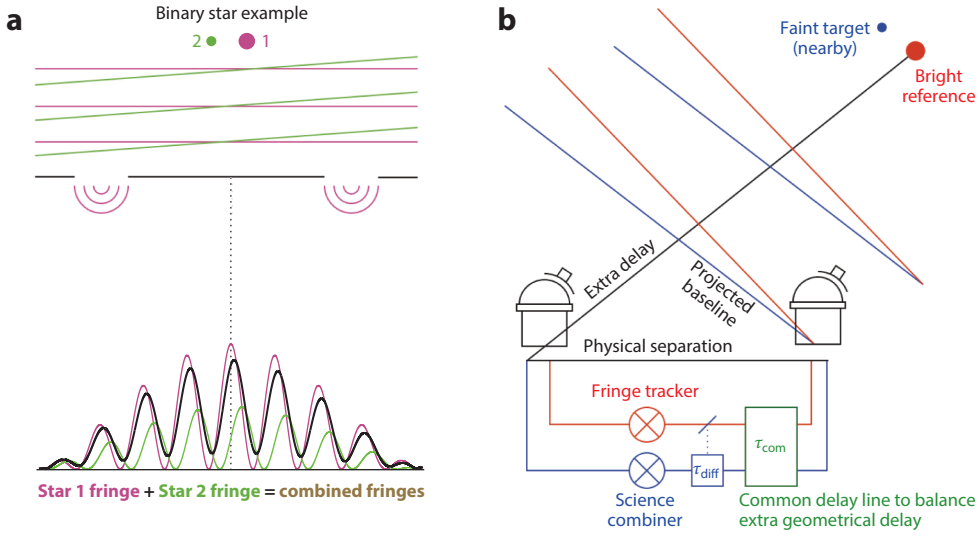

Figure 8

Young's two-slit experiment illustrates (*a*) the basics of optical interferometry. Each part of a distant source (*red*+*green*) creates its own fringe that incoherently adds together (*black*). (*b*) The basic elements of a practical ground-based dual-beam interferometer. Light from two fields is delayed together (τ_{common}) to account for common geometrical delay and then split to allow differential delay ($\tau_{\text{differential}}$). The reference starlight (*red*) is detected at the fringe-tracking combiner, and the derived atmospheric delays are then fed back to the common delay line, allowing longer coherent integration on the science combiner (*blue*). This is analogous to a wave front sensor/deformable mirror in a natural guide star adaptive optics system.

coherent field of view matches the telescope diffraction limit for a spectral resolution $R = \frac{B}{D}$, which is typically the lowest fractional bandwidth used in practical interferometers.

3.2. Complex Visibilities

When an interferometer looks at a complex object, the interference pattern changes with respect to that of a point source. **Figure 8*a*** illustrates the basic principle. Each point of light on the distant source creates its own interference fringe slightly shifted with respect to the others, because the wave fronts are slightly tilted, and with an intensity proportional to the brightness of each part of the source. Because astronomical sources are incoherent, these two sine waves add up in power, resulting in a sine wave that is characterized by a fringe amplitude and phase. The normalized amplitude of the fringe is called the contrast or the visibility V, where unity means the fringe is fully modulated, creating dark destructive nulls and bright constructive peaks; a zero visibility shows no modulation across the interferogram. O/IR interferometrists have historically used this normalized visibility because the total flux is often poorly measured. Radio astronomers use the coherent flux instead—the total flux times the normalized visibility—with units of flux density (W m^{-2} Hz^{-1}), and this practice is becoming common for some IR applications when the normalization is problematic, for example, in the thermal IR. The relative position of the fringe gives the phase ϕ of the interference. The combination of the two quantities visibility amplitude V and phase ϕ forms the complex visibility $\tilde{V} = Ve^{i\phi}$.

Interpreting this complex visibility is straightforward. Because each point on the sky creates a sine wave, the final observed complex visibility $\tilde{V}$ is simply an integral of sky intensity times sine waves, otherwise known as a Fourier transform. This relationship is captured by the

van Cittert–Zernike theorem: $\tilde{V}(u,v) \propto \int_{\text{sky}} I(\alpha,\delta) e^{-2\pi i(u\alpha+v\delta)} \mathrm{d}\alpha \mathrm{d}\delta$, where $I(\alpha, \delta)$ represents the target brightness distribution on the sky as a function of right ascension (α) and declination (δ), and (u, v) represents the projected baseline in units of the observing wavelength along (east, north) directions.

Fried parameter, r_0: diameter for which the root-mean-square (rms) wave front error introduced by the atmosphere is 1 rad

3.3. Atmospheric Coherence Lengths and Times

In order to translate the elegant principles of interferometry to a practical facility, we must also account for properties of the atmosphere. In this section, we introduce the basic picture with further elaboration in Section 5, and refer the reader to a more in-depth treatment by Roddier (1981) and Quirrenbach (2000).

The ideal picture of an interferometer starts to break down when we consider light propagating through the atmosphere. The perfectly flat wave fronts at the top of the atmosphere become distorted as they encounter varying densities of air. Simplistically, we can follow each ray and add up the time delay caused by the index of refraction of air. Rays close together go through essentially the same air and so have small root-mean-square (rms) variation, whereas rays far apart become more different. The Fried parameter r_0, or atmospheric coherence length, is defined as the diameter of the circular aperture that has an average rms wave front error of 1 rad in phase. This value is wavelength dependent because the phase depends on wavelength and the index of refraction varies some with wavelength. The theory of Kolmogorov turbulence predicts that $r_0 \propto \lambda^{\frac{6}{5}}$, and that telescopes with diameters $D > r_0$ will have long-exposure images with seeing-limited angular resolution $\theta_{\text{seeing}} = \frac{\lambda}{r_0} \propto \lambda^{-\frac{1}{5}}$. Thus, seeing-limited image quality improves into the IR counter to the diffraction-limited performance. Sites with excellent seeing will have $r_0 \approx$ 20 cm in the visible (500 nm) and $r_0 \approx 1$ m at K band (2.2 μm). As explained below, the limitation of r_0 can be overcome by including AO.

Most observations in astronomy have long exposure times, i.e., minutes or even hours. For interferometry, this is only possible when actively stabilizing the fringes to well better than a wavelength, a technique called fringe tracking (Section 5.3). Otherwise, the turbulent atmosphere causes time-varying optical path lengths above each telescope and a changing phase of the interference fringe. As the phase changes, the troughs and peaks blur together in a long exposure ruining the measurement. Thus, interferometers must observe fringes with short exposure time to freeze the atmospheric motions. It is useful, though incomplete, to adopt Taylor's frozen atmosphere hypothesis, which assumes the wave front errors are fixed as they are blown across the telescope aperture at a wind velocity v. If so, then the typical coherence time is given by $\tau_0 = \frac{r_0}{v}$. For upper atmosphere speeds of 10 m s^{-1}, we find $\tau_0 \approx 20$ ms in the visible at excellent sites, though jet stream speeds of $>$50 m s^{-1} can drastically reduce the coherence time to $<$3 ms. Again, note the coherence time will be much improved in the IR compared to visible due to the dependence on r_0.

Combining r_0 and τ_0 leads to the concept of a coherent volume of photons that can be used for estimating sensitivities. Without AO and fringe tracking, the largest useful aperture is r_0 and the longest coherent integration time is τ_0; thus, the photon volume is proportional to $r_0^2(c\tau_0) \propto \lambda^{3.6}$, according to Kolmogorov turbulence. This strong dependence on wavelength explains why IR interferometry has been much more developed than visible light interferometry. Section 5 shows how advanced methods now can largely overcome this traditional limitation to interferometry sensitivity, boosting fringe sensitivity by over 1,000 times in the past 10 years.

3.4. Practical Implementation

Although the monolithic binocular mount of the LBTI resembles Young's two-slit configuration, most interferometers are an abstraction of this experiment. The apertures are replaced by telescopes that must be corrected by AO or be limited to a size $\approx r_0$. Once corrected, light from

Phase tracking: maintaining the optical path difference to within 1 rad of phase delay

each telescope is sent to the delay lines. The wave fronts for each telescope must be dynamically delayed based on the sky position of the target because wave fronts arrive obliquely, intercepting some telescopes before others. In order to measure an interference fringe, the optical path difference (OPD) between telescopes must be stabilized either within a coherence length using group-delay tracking or within 1 rad by phase tracking, the latter allowing long coherent integrations. For wide-field phase referencing (separation >10 arcsec; only at VLTI), the light from the reference and science targets must be split at the telescope and sent through the delay lines on separate beams. Along the way, we must seek to minimize any differential dispersion and birefringence while maintaining high transmission. With typically more than 20 surfaces from the telescope up to the instrument, the beamtrain transmission alone is typically low (<20% in IR, <10% in visible). Once the OPDs and differential polarization (e.g., by half- and quarter-wave plates) have been compensated for, all the beams can now be interfered. **Figure 8*b*** illustrates these basic components of today's interferometers.

Beam combiners fall into two general categories: all-in-one or pairwise. As the name implies, an all-in-one combiner will overlap light from several telescopes together, creating many fringes simultaneously. To distinguish different baselines, the interference patterns are either coded spatially (e.g., in image-plane) or modulated temporally. In a pairwise combiner, the light is split up and combined in pairs, so each combiner only has two input beams. Also here, the interference can be scrutinized either with temporal modulation using a beam splitter or through a so-called ABCD combiner, which further splits the beams and adds an extra combiner to allow four quadrature fringe phases to be measured simultaneously. The ABCD quadrature can also be achieved by temporal modulation and reading the detector at four fixed phase shifts. CHARA/MIRC-X is an example of an all-in-one combiner, VLTI/GRAVITY is an example of a pairwise combiner using the ABCD method, and NPOI/CLASSIC combiner combines aspects of both.

In order to improve calibration of fringe coherence, most combiners apply some kind of spatial filtering to remove aberrations from the incoming beams before interference. The purest way to do this is by using single-mode waveguides such as small-core fibers or planar waveguides, although pinholes can also be used (e.g., VLTI/MATISSE) when no fibers are available. During this process, the single coherent flux can fluctuate wildly with atmospheric turbulence, although AO improves this. For calibration, the coupling fraction into the single mode must be monitored in real time. The FLUOR (Fibered Linked Unit for Optical Recombination) combiner on IOTA (Coudé du Foresto et al. 1998) pioneered the use of single-mode waveguides for interferometry, and many combiners today now are based on this breakthrough [e.g., NPOI/VISION (Visible Imaging System for Interferometric Observations at NPOI); CHARA/FLUOR, SPICA (Stellar Parameters and Images with a Cophased Array), MIRC-X, MYSTIC (Michigan Young Star Imager at CHARA); and VLTI/PIONIER (Precision Integrated-Optics Near-infrared Imaging ExpeRiment), GRAVITY]. In Section 4.2, we discuss how the miniaturization made possible by telecommunication technologies has enabled a new generation of sophisticated instruments.

3.5. Closure Phases, Phase Referencing, and Fringe Tracking

Although a fringe measurement reveals an amplitude and a phase, the fringe phase is initially corrupted by atmospheric turbulence. A time delay $\Delta\tau$ above one telescope due to a change in air density along the path of the photons will shift the phase of the fringe by $\phi_{\mathrm{rad}} = 2\pi \frac{c\Delta\tau}{\lambda}$, and this changes by 1 rad every coherence time $\tau_0 \ll 1$ s. The phase excursions are too large and the statistics not sufficiently stationary to allow long-term averaging. Two-telescope interferometers only average the $|\tilde{V}|^2$ and fit models to estimate stellar diameters or binary parameters. Complex astrophysical objects encode much information in the Fourier phases, and so there is the need to calibrate these atmospheric fluctuations in order to carry out true imaging with interferometers.

Radio interferometry encountered this phase instability problem first and introduced the concept of closure phase (Jennison 1958), which is an observable quantity for a triangle of baselines and which is immune to phase instabilities. The concept was introduced in the optical regime by Lohmann et al. (1983). Any fringe phase shift related to a single telescope (not baseline) can be removed by adding up fringe phases in a closed triangle. This can be seen by realizing that phase shift at telescope 2, for instance, will cause an equal but opposite-signed shift for baseline $1 \rightarrow 2$ and baseline $2 \rightarrow 3$. Closure phases thus reveal linear combinations of the true fringe phases we need for modeling and image reconstructions but not all the information. Numerically, the number of independent phases in an N telescope interferometer is $N(N-1)/2$, whereas the number of independent closure phases is $(N-1)(N-2)/2$. For example, a 3-telescope array accesses one closure phase out of three phases, a 6-telescope array (CHARA) accesses 10 out of 15 phases, and a 50-telescope array (ALMA) measures 1,176 out of 1,225 phases. For more detailed explanations and examples, see the thorough treatment by Monnier (2000). Here, we summarize a few important properties of closure phases compared to Fourier phases. First, astrometric information is lost within closure phases because an image shift on the sky is equivalent to adding a planar geometrical delay above each telescope, thus canceling out in a triangle. Point-symmetric distributions (like uniform stars or simple inclined disks or rings) have phases of 0 or π when the origin is centered on the object, thus closure phases of point-symmetric objects also can only be 0 or π. Closure phases provide absolutely crucial information for asymmetric objects and can be interpreted with forward modeling (Section 4).

Although closure phases allow recovery of phase information, their use does not extend the coherence time and thus does not overcome the sensitivity limitations from short exposures. Phase referencing can be used to allow much greater sensitivity by using a bright nearby star as a phase reference, a kind of AO for interferometry that is used extensively in the radio band. This technique has limits because it requires finding a reference star within the isopistonic patch, which is the patch of sky that sees the same turbulence; the wave fronts from stars more than $\approx$30 arcsec away (in NIR) encounter different turbulence and thus the phase errors are mostly uncorrelated. Although phase referencing was demonstrated on the Keck Interferometer shortly before being shut down (Woillez et al. 2014), the VLTI/GRAVITY instrument was the first to make the technique practical and is leading us into a new era of high-sensitivity observations—see science highlights in Section 2 along with more technical details in Section 5.

More common than dual-beam phase referencing is fringe tracking using self-referencing. Here, one uses part of the light of the target to track the fringes while reserving some of the light for science observations. For instance, at the Keck Interferometer, light from one side of the beam splitter was sent to the low-resolution spectrograph for high-sensitivity fringe tracking, whereas the light from the other side of the beam splitter was sent to a high-resolution spectrometer (Woillez et al. 2012). Often one wavelength channel is used for real-time fringe tracking to allow integration at another wavelength [e.g., Keck Nuller, VLTI/FINITO (Fringe tracking Instrument of Nice and TOrino), CHARA/CHAMP (CHARA Michigan Phase-tracker); Gai et al. 2003, Monnier et al. 2012, Serabyn et al. 2012]. The VLTI/GRAVITY fringe tracker (Lacour et al. 2019) allows long integrations at K band or with the MATISSE instrument in L, M, and N bands. Note that the fringe phases do not need to be tracked on all baselines because a long-baseline fringe (say, among telescopes 1–3) can be stabilized as long as fringes of two connecting shorter baselines ($1 \rightarrow 2$ and $2 \rightarrow 3$) are available; this technique is called baseline bootstrapping.

3.6. Homodyne, Heterodyne, Intensity, and Quantum-Enhanced Interferometry

We conclude this section with a short summary of different kinds of interferometry under active development. In Section 1, we already introduced the main technique of direct detection or

homodyne detection in which the light from the different telescopes is interfered before detection by a square-law detector, which measures the intensity = |amplitude|^2. This is by far the most common way optical interferometry is carried out today.

A modified version of this method involves up-converting the light at each telescope to higher frequency using nonlinear optics (e.g., Boyd & Townes 1977, Baudoin et al. 2016). This up-converted light can then be interfered using traditional direct detection methods, potentially with advantages in the thermal IR, where fiber optics and detectors are inferior to shorter-wavelength devices.

Heterodyne interferometry (Johnson et al. 1974, Hale et al. 2000) has been a practical method requiring only local measurements at the telescopes by mixing with a carrier signal and with interference happening separately. Often, the information can be recorded with correlation happening "in software," or using special-built digital correlators. Heterodyne interferometry in the visible, NIR, and MIR bandwidths is intrinsically much less sensitive than direct detection as it involves mixing the starlight with a bright laser as a local oscillator, introducing laser shot noise as a background that becomes severe at wavelengths shorter than 20 μm. See Ireland & Monnier (2014) for recent comparison of heterodyne and homodyne sensitivity in the context of the MIR Planet Formation Imager (PFI) project and Berger et al. (2020) for plans to radically increase bandwidths using multiplexing.

As already mentioned, intensity interferometry measures correlations in photon arrival times at different telescopes and is one of the earliest true quantum optics discoveries (Brown & Twiss 1956). This correlation requires two photon processes and thus is intrinsically less sensitive than homodyne methods, though again can be possibly practical for some applications. Attempts to revive this technique are under way, taking advantage of the large collecting area and baselines from current and next-generation Cherenkov gamma-ray telescopes and optical telescopes at Calern as well as on the ATs of the VLT (Nuñez et al. 2012, Guerin et al. 2017, Cherenkov Telesc. Array Consort. et al. 2019) and advances in detectors for extreme wavelength multiplexing (Horch et al. 2013).

The latest frontier to open up in optical interferometry is using quantum resources, such as entangled photons, to confer a quantum advantage. Using entangled photons as a QLO, Gottesman et al. (2012) showed the laser shot noise of conventionally heterodyne interferometry can be sidestepped, recovering similar sensitivity of today's direct detection methods but with potentially important practical advantages in the future. Brown et al. (2022) recently reported a first lab demonstration of quantum advantage using heralded quantum-entangled photons, and others have speculated on advantages for quantum-enhanced interferometry in a future world with quantum networks and quantum hard drives (e.g., Bland-Hawthorn et al. 2021).

3.7. Software Tools and Resources

A host of community tools exist to help interferometrists prepare observations, analyze data, make images, and search archives. The Jean-Marie Mariotti Center (**http://jmmc.fr**) is a clearinghouse of essential software resources including `searchCal` for finding calibrators, `Aspro` for planning observations at any facility, `LITpro` for fitting simple models, `OImaging` for image reconstruction tools, `BadCal` for a bad calibrator list, and the `OiDB` for archiving and searching for reduced data. New Python-based `PMOIRED` (Mérand 2022) also can fit a range of models as can `Julia`-based `SQUEEZE` and `OITOOLS` (**https://www.chara.gsu.edu/analysis-software/imaging-software**). All these tools use the OIFITS standard for exchanging calibrated optical interferometry data (Pauls et al. 2005, Duvert et al. 2017).

3.8. Interferometry Primer: Summary Points

1. A long-baseline interferometer is a Young's two-slit experiment, which measures Fourier components of the object brightness distributions.
2. Today's facilities have best angular resolution ranging from 0.5 to 5 mas.
3. Atmosphere turbulence poses fundamental limitations that can be overcome using closure phases, AO, fringe tracking, and dual-beam phase referencing.

UV plane: the projected interferometer baselines (East, West) in units of observing wavelength, associated with the measured visibility points

4. ADVANCES IN INTERFEROMETRIC IMAGING

The past decade has seen a breakthrough in not only sensitivity but also imaging power. It is striking that most of the results we highlight in Section 2 are images and not visibility curves, a huge change from previous reviews of O/IR interferometry. In this section, we outline how this was made possible through effective use of 4- and 6-telescope arrays, new beam combiners that use all telescopes simultaneously, better beam combiner architectures to enhance calibration precision and data throughput, and also mature and proliferating image reconstruction software.

4.1. Filling the UV Plane

The O/IR interferometry field currently has three major imaging interferometers, NPOI (reconfigurable 6T), CHARA (fixed 6T), and VLTI-ATs (reconfigurable 4T)/VLTI-Unit telescopes (UTs; fixed 4T). This is reminiscent of the pre-ALMA age of millimeter-wave interferometers when many small arrays existed with <10 telescopes (Sargent & Welch 1993). The number of baselines in an N-telescope interferometer is $N(N-1)/2$ (Section 3.5); thus, even adding a few telescopes can substantially transform the imaging capabilities. Because each projected baseline is a single Fourier component of the true sky image, the imaging fidelity of an array is directly related to the ability to fill the UV plane. In addition to simply increasing the number of telescopes, we can improve UV coverage by (*a*) using Earth's rotation to sample different baseline projections, (*b*) employing movable telescopes at the same site and combining configurations (as long as object does not change in time), (*c*) combining data from geographically different interferometers at nearly the same time, and (*d*) observing over a wide wavelength range to sample different resolutions when coupled with a wavelength-dependent model of source. **Figure 9** shows the evolution of UV coverage over past decades.

Even when arrays were built with four or more telescopes, beam combiners did not yet exist to combine all the beams at the same time. This was the case for NPOI, VLTI, and CHARA, which did not possess combiners that could measure all baselines and closure phases simultaneously until the past decade, often a decade after first light. One part of the delay was caused by the cumbersome prospect of creating a 4+ beam combiner in bulk optics, which would take up large optical tables and require ongoing tedious alignments. As already covered above, the classic pairwise beam combiner works well for two or three telescopes; however, it scales poorly for a large number of telescopes. Light from each of N telescopes must be split $N-1$ ways and then combined with all other beams on $\binom{N}{2}$ beam splitters leading to $N(N-1)$ outputs. Furthermore, bulk optics combiners historically have not produced calibration that is as precise as those using single-mode waveguides.

4.2. Better Calibration and Miniaturization with Single-Mode Waveguides

We already mentioned the breakthrough in calibration from single-mode fibers and evanescent wave fused couplers (e.g., IOTA/FLUOR; Coudé du Foresto et al. 1998, Perrin et al. 1998) in the 1990s, but this architecture did not lead to all-fiber beam combiners for imaging. This was due

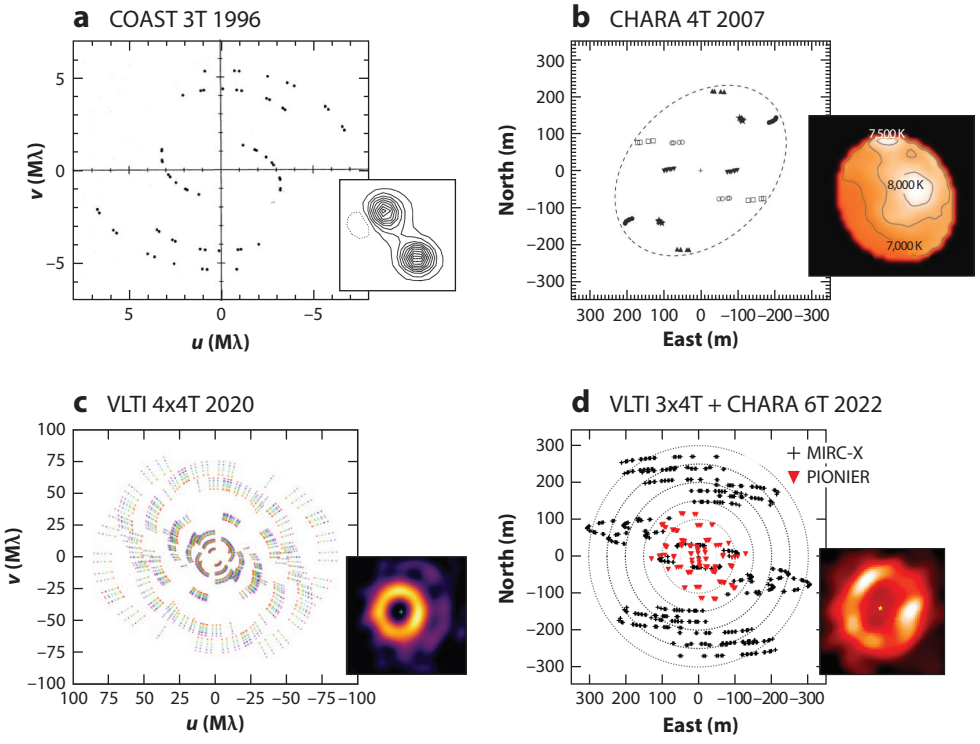

Figure 9

The UV plane can now be densely filled using multiple configurations of four- and six-telescope arrays. The evolution over the past 20 years has been dramatic, and we show here actual published UV coverage along with the reconstructed images. Panel *a* adapted with permission from Baldwin et al. (1996); copyright 1996 ESO. Panel *b* adapted from Monnier et al. (2007); copyright 2007 AAAS. Panel *c* adapted from Kluska et al. (2020b); copyright 2020 ESO. Panel *d* adapted from Ibrahim et al. (2023). Abbreviations: CHARA, Center for High Angular Resolution Astronomy array; COAST, Cambridge Optical Aperture Synthesis Telescope; MIRC-X, Michigan InfraRed Combiner-eXeter; PIONIER, Precision Integrated-Optics Near-infrared Imaging ExpeRiment; VLTI, Very Large Telescope Interferometer.

to the difficulties in constructing a network of fiber-based splitters and couplers while maintaining better-than-millimeter internal path lengths and controlling for differential dispersion and birefringence.

This engineering problem was first solved using planar waveguide circuits (Kern et al. 1997), developed initially for telecommunications (see a recent review by Righini & Chiappini 2014). In analogy to integrated circuits, IO allows complex optical functions such as splitters, combiners, achromatized phase delays, and active phase modulation to be embedded in a thin dielectric slab using lithographic methods. The first IO device used for astronomy was IOTA/IONIC (Integrated Optics Near-Infrared Interferometric Camera; Berger et al. 2001), and this technology has since matured with a basic form in which the input beams are split, are recombined to form all interference pairs, and have internal delays to sample four equally spaced fringe phases. The IO outputs are in a line that can then be dispersed onto an array detector. This so-called pairwise ABCD IO combiner is the basis for the *H*-band 4T combiner VLTI/PIONIER (Le Bouquin et al. 2011), the *K*-band 4T combiner VLTI/GRAVITY (Perraut et al. 2018), the *K*-band 4T combiner CHARA/MYSTIC-ABCD, and the new *H*-band 6T combiner for the CHARA/SPICA fringe

tracker. IO devices rarely can operate beyond ≈30% spectral bandwidth (due to the requirement to have low bending losses while maintaining high single-mode purity); thus, each astronomical band (*J*,*H*,*K*) needs its own device. Material absorption and scattering losses in the visible and thermal IR have limited IO use in these wave bands. Due to the need to minimize the curvature of waveguide bends, the chip length scales like N^2, incurring significant propagation losses (≈50%) for current devices. Better materials and new writing techniques continue to be developed in this active area; for instance, see further discussion on nulling in Section 6.6 and the recent advances in 3D laser writing (e.g., Labadie et al. 2018), which promises more compact combiners in more materials as the writing quality improves.

Nulling: using destructive interference to cancel the light from a point source in one of the beam combiner outputs, thereby reducing the photon noise

Another influential beam combiner architecture tailored for imaging with large N telescopes uses image-plane combination of light that has been spatially filtered by fibers but with beam combination in the image-plane using conventional bulk optics. The CHARA/MIRC combiner pioneered this method, using conventional telecom fibers installed in a nonredundant linear array within a silicon V-groove mated with a microlens array. The interference fringes can then be focused onto a slit and dispersed, as for the IO devices. Bending losses tend to limit the usable bandwidth of IO devices, whereas single-mode fibers can have high transmission over ≈50% spectral bandwidths, for instance, including 1.1–1.8 μm using standard telecom fibers or 1.5–2.4 μm using special low-OH silica or fluoride fibers. This style of combiner is limited to wavelengths where good fibers exist. The image-plane combiner is also susceptible to cross talk (Mortimer & Buscher 2022). So-called MIRC-style combiners lie at the heart of current instruments MIRC-X (Anugu et al. 2020), MYSTIC (Setterholm et al. 2022), SPICA (Mourard et al. 2018) and VISION (Garcia et al. 2016). **Figure 10** shows schematics of both IO and MIRC-style combiners and how the dispersed interference patterns look in practice.

4.3. Advanced Image Reconstruction Algorithms

Many of the highest profile results in O/IR interferometry would not have been possible without advances in image reconstruction algorithms, beyond those developed by the radio community. Here, we describe the current state-of-the-art but demur from detailed derivations or anything resembling a "how-to." We refer interested readers to the review of methods by Baron (2016), 2020), along with tutorial-like presentation by Thiébaut & Young (2017). Here, we provide a brief overview of the current algorithms and future directions.

The radio community was first to attempt interferometric imaging and had initially been quite innovative in developing algorithms to account for the limited UV coverage of early facilities. The `CLEAN` (Högbom 1974) algorithm was tractable even with early computers and subsequently built into the standard radio packages `AIPS` and `CASA`. The basic principle behind `CLEAN` is to take a direct Fourier transform of the complex visibilities in the (mostly empty) UV plane, then to follow this with a deconvolution step to remove the large sidelobes that appear in the initial image. Because most of the artifacts come from the large known gaps in the UV plane, this method works well for simple objects, especially when consisting of mainly point sources like binary or triple systems. Closure phases are incorporated using an iterative self-calibration scheme, applying positivity and limited field-of-view windows when carrying out the deconvolution (Readhead & Wilkinson 1978). Unfortunately, `CLEAN` does a poor job with reconstructing smooth extended emission, does not intrinsically deal with error bars or closure phases, and smooths away details as a way to minimize artifacts. The flaws of `CLEAN` are most severe with small $N < 10$ arrays like we have in O/IR interferometry.

Faster computers now allow a more mathematically rigorous approach. The forward modeling approach considers all possible astronomical images as hypotheses and then choose the best set of

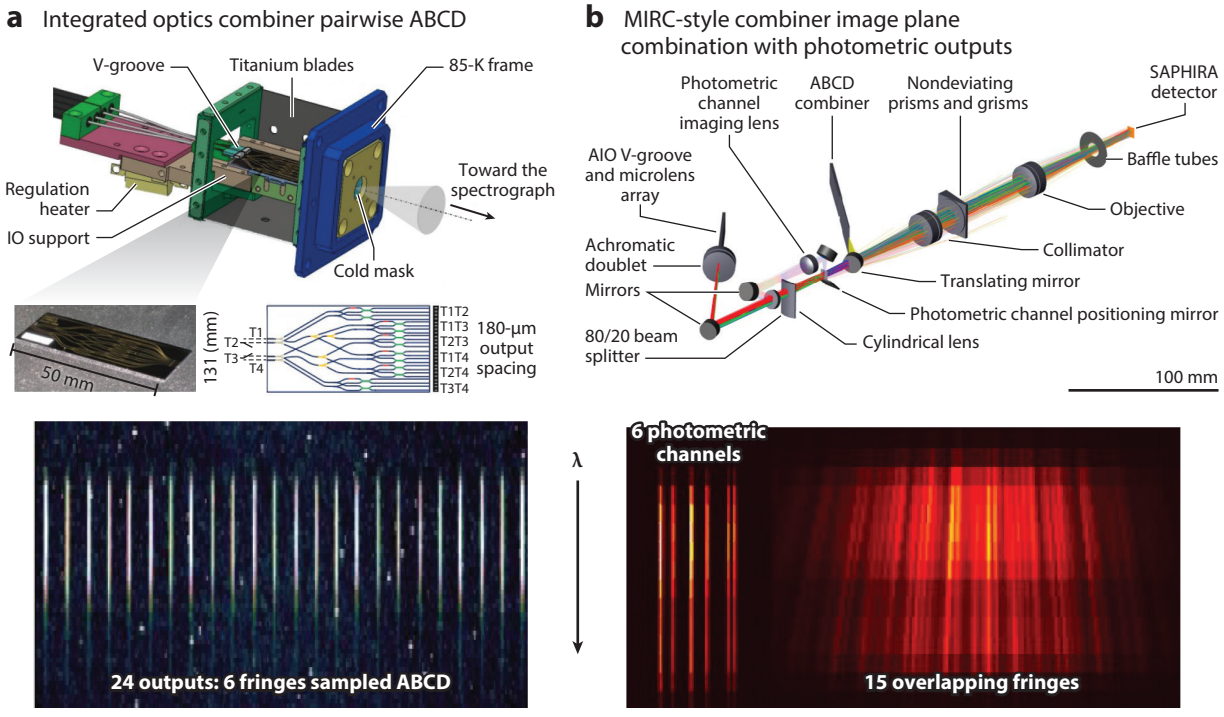

Figure 10

The imaging breakthroughs of the past decade required a new generation of imaging combiners. Today's imaging instruments have all adopted either a pairwise ABCD combiner using integrated optics or an MIRC-style instrument using image-plane AIO combination following single-mode fibers. Panel *a* shows the VLTI/GRAVITY instrument; panel *b* shows the CHARA/MYSTIC instrument. Panel *a* adapted with permission from Perraut et al. (2018); copyright 2018 ESO. Panel *b* adapted from Setterholm et al. (2022). Abbreviations: AIO, all-in-one; CHARA, Center for High Angular Resolution Astronomy array; IO, integrated optics; MIRC, Michigan InfraRed Combiner; MYSTIC, Michigan Young Star Imager at CHARA; SAPHIRA, Selex Advanced Photodiode HgCdTe Infrared Array; VLTI, Very Large Telescope Interferometer.

images based on a combination of the best fit to the observables (χ^2) as well as any prior information, such as positivity, known field of view, etc. This is an example of an ill-posed inverse problem with no unique solution, so one must regularize the solution by introducing additional constraints. The first widely adopted regularizer was the Maximum Entropy Method (MEM; Gull & Skilling 1984) which attempts to maximize the so-called entropy S of the image: $S = -\sum_i f_i \log \frac{f_i}{p_i}$, where f_i is the fraction of flux in pixel i, and p_i is the Bayesian prior (often taken as constant). Conceptually, we expect this to find the smoothest possible image consistent with the data, which is attractive for the astronomical utility.

Regularizer: a mathematical metric that is optimized when fitting interferometric data with a model image

The panoply of codes now available often incorporate alternative regularizers to entropy, which go by a variety of names such as "total variation," "uniform disk regularizer," and "dark energy," some of which prefer sharp edges while others select smooth edges. Thus the astronomer is now expected to choose the regularizer appropriate to their target (Renard et al. 2011). Another way to approach image reconstruction is through compressed sensing, in which one tries to find a good-fitting image that has the fewest components, where a component can be something like a wavelet coefficient or derived from a dictionary of radiative transfer calculations.

Today's image reconstruction frontier involves regularizing across time to track moving blobs in dust shells and disks, regularizing across wavelengths to improve UV coverage but accounting

for smooth changes in images with wavelength, and even imaging with a (latitude, longitude) pixel grid projected onto a rotating spheroid to better image spots on spinning stars. Kluska et al. (2014) outlined a widely used approach in which a central star with a known size and spectrum can be combined with a dust image that can have a different spectrum but is otherwise gray. This SPARCO (semi-parametric approach for image reconstruction of chromatic objects) method is needed for imaging disks around young stars in which the flux ratio between star and disk varies substantially across wavelength channels.

Radio work on imaging with sparse UV coverage radically slowed in the 1990s, and the IAU Working Group on O/IR Interferometry began a series of meetings around 2000 to address the need for better imaging as the modern facilities were building up. These meetings led to the OIFITS data standard (Pauls et al. 2005, Duvert et al. 2017) for calibrated optical interferometry data, as no appropriate standard from radio existed. In addition, a series of image reconstruction contests have been held during the SPIE (Society of Photo-Optical Instrumentation Engineers) astronomical instrumentation conference every two years since 2004 to encourage development of advanced imaging methods and to recognize excellent contributions. These double-blind contests typically used simulated data based on existing facilities and instruments with realistic noise (e.g., Lawson et al. 2004) or even were attempted on real data (Monnier et al. 2014). The result has been an innovative and dynamic subfield that has produced a range of community tools, usually publicly available: `BSMEM` (Buscher 1994), `MACIM` (Ireland et al. 2006), `MiRA` (Thiébaut 2008), `IRBis` (Hofmann et al. 2014), `WISARD` (Le Besnerais et al. 2008), `SQUEEZE` (Baron 2016), `SURFing` (Roettenbacher et al. 2016), `ROTIR` (Martinez et al. 2021), `ORGANIC` (Claes et al. 2020), and `G`$^{\mathtt{R}}$ (GRAVITY Collab. et al. 2022a). This work has now fed back to radio interferometry, informing the imaging approach of the EHT project (e.g., Lu et al. 2014).

4.4. Advances in Interferometric Imaging: Summary Points

1. Interferometric imaging requires as many telescopes as possible to fill the UV plane.
2. Within the past decade the major facilities have been able to combine all their available telescopes, with single-mode optics at the core of today's beam combiners.
3. Specialized image reconstruction algorithms have been developed for O/IR interferometry, advancing the field over earlier work by radio astronomers.

5. BREAKTHROUGH IN SENSITIVITY

Initially, astronomical interferometers were made from small-aperture telescopes or siderostats with a diameter less than a few times the atmospheric Fried parameter r_0. The sensitivity advantage of large telescopes for interferometry was recognized early on, and both the VLT (Léna 1979, Beckers et al. 1990) and Keck telescopes (Colavita et al. 1998, 2013) have been designed and implemented to also operate as interferometers. The use of AO then increases $r_0 \approx 0.1...1\,\mathrm{m} \rightarrow D \approx 10\,\mathrm{m}$; i.e., the coherent volume $r_0^2(c\tau_0)$ (Section 3.3) increases by a factor of $\gg$100, such that fringes of moderately faint objects $m_\mathrm{K} \approx 10...11$ mag can be detected within the atmospheric coherence time $\tau_0 \approx$ a few milliseconds. This allows for stabilizing the fringes, and thereby opens up, by a factor of 1,000–100,000 longer, exposures times approaching $T_\mathrm{exp} \approx$ minutes–hours, and reaching out for yet another factor of 1,000 fainter objects $m_\mathrm{K} \approx 19$ mag by dual-beam interferometry.

However, the technical hurdles were substantial, and it was only GRAVITY that brought all techniques together for routine science operation. **Figure 11** illustrates the complexity and major subsystems of such a modern interferometer.

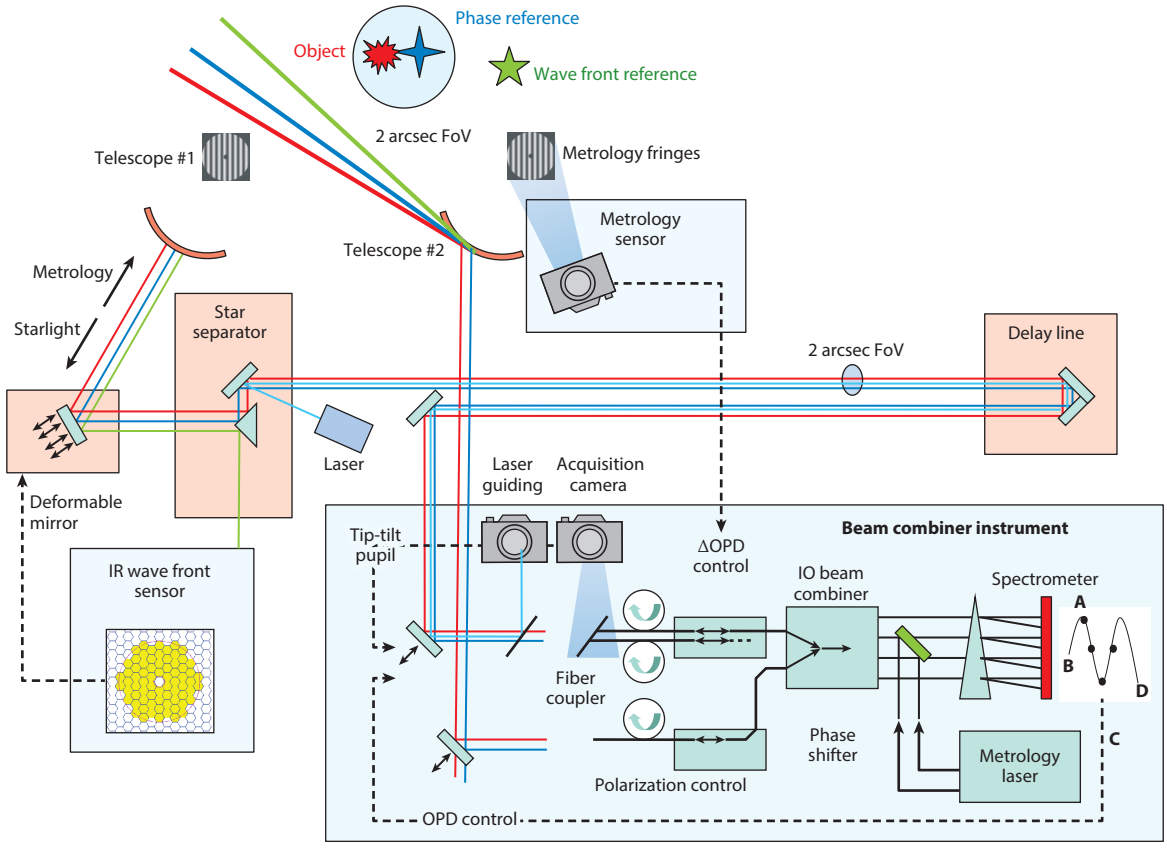

Figure 11

Overview and working principle of a modern, large telescope interferometer at the example of GRAVITY. Each telescope is equipped with AO to provide a diffraction-limited beam, which is then transported through mirrored delay lines to the beam combiner instrument. The instrument provides two beam combiners, one for fringe tracking, the other optimized for long exposure, high spectral resolution interferometry of the science target. Off-axis fringe tracking is done by separating the phase reference and science target at either the instrument level (narrow field of view) or the telescope level (wide field of view). In the latter case the two beams are propagated separately to the beam combiner instrument. The optical path length within the observatory is controlled via several laser metrology systems, delay lines, and differential delay lines. The beams are stabilized through active field and pupil tracking, again taking advantage of laser metrology. For clarity, we show only two telescopes, and one AO, delay line, and beam combiner.
Figure adapted with permission from GRAVITY Collab. et al. (2017a); copyright 2017 ESO. Abbreviations: AO, adaptive optics; FoV, field of view; IO, integrated optics; OPD, optical path difference.

5.1. Sensitivity Gain from Large Telescopes

On top of collecting area, large telescopes present many more fundamental advantages for interferometry. They arise from phase-averaging effects across the aperture, which increase the characteristic timescales for fringe tracking, and from a smaller diffraction limit, thereby enabling the observations of crowded regions. In the following, we quantify each respective advantage, which when taken together yield a large-telescope advantage $\propto D^{2\ldots5}$.

The SNR in observations of point sources increases with the telescope diameter $\propto D^2$ for background-limited, single-mode interferometric observations (Beckers et al. 1990). The reason is that the thermal background for diffraction-limited observations is irrespective of telescope size (étendue = collecting area × receiving solid angle = λ^2), whereas the signal increases $\propto D^2$, i.e.,

by a factor of 100 when going from 1- to 10-m telescopes. At the same time, the telescope primary beam shrinks in area with telescope diameter $\propto D^{-2}$. In the crowding limit, the number of objects in the observed field of view is reduced by a factor $\propto D^2$, and therefore the SNR per object increases accordingly $\propto D^2$, i.e., by another factor of 100 when going from 1- to 10-m telescopes.

For observations of crowded fields in the IR, which are limited by both the thermal background and crowding, the SNR increases $\propto D^4$. This holds for interferometry as well as for diffraction-limited observations with single telescopes. In O/IR interferometry with its comparably poor UV coverage, the smaller field of view can be even more decisive for the observation of complex scenes. For the Galactic Center, e.g., the stellar density is about 70 stars brighter than 19.5 mag within the diffraction-limited field of view of a 1-m-diameter telescope, too many for the sparse UV coverage of a 4-telescope interferometer. It is the factor of 100 smaller diffraction area of 10-m telescopes, which reduces the complexity to a few stars per pointing and thereby allows for the deep imaging and the accurate astrometry presented in Section 2.3.

Next, the coherence time increases with telescope diameter, because single-mode interferometers are probing the average phase of the pupil, thereby smoothing out the temporal fluctuations (**Figure 12*a***). The increase in coherence time is $\propto D^{1/6}$ for a moderate-size telescope $r_0 \ll D \ll L_0$ (Kellerer & Tokovinin 2007), and $\propto D^{7/6}$ when D approaches the outer scale of turbulence L_0. However, current telescopes ($D \lesssim 10$ m) are smaller than L_0 (typically a few tens of meters for good astronomical sites; Ziad 2016), and take only moderate advantage of the increased coherence time. The more relevant advantage comes from the shape of the phase power spectrum (**Figure 12*b***): The averaging effect leads to the suppression of especially the high-frequency perturbation and results in a turnover of the atmospheric Kolmogorov power spectrum at a frequency $\approx 0.3\,\frac{v}{D}$ (Conan et al. 1995), where v is the wind speed. This cutoff frequency is reflected in the required control bandwidth of the fringe tracker, which in turn is ultimately set by the detector integration time.

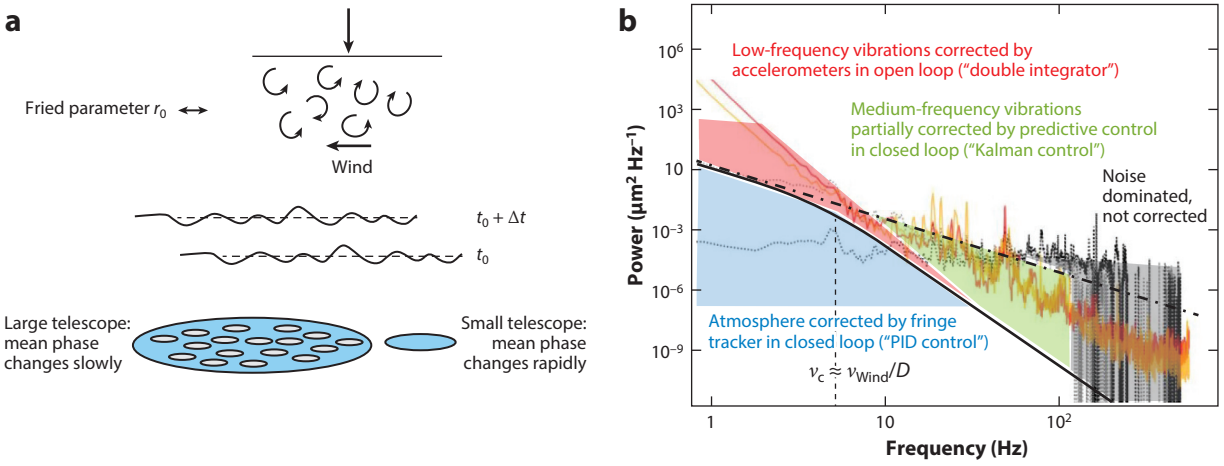

Figure 12

Interferometry with large telescopes. (*a*) Large apertures average out the small-scale atmospheric perturbations, thereby increasing the coherence time as compared with a small telescope. The resulting temporal power spectrum (*b*) of the mean phase (*solid black curve*) exhibits a break around a typical frequency of $\approx \frac{v}{D}$, where v is the wind speed, and D is the telescope diameter. Vibrations (*red* and *yellow lines*) exceed the atmospheric path length fluctuations for large telescopes. They are corrected by a combination of accelerometers (*open loop control*) and fringe tracking (*closed loop*) for low and intermediate frequencies up to a few tens of hertz. Vibrations at higher frequencies—especially from optics not monitored by accelerometers—can be partially corrected by predictive control with the fringe tracker, but ultimately they limit the current fringe-tracking residuals (*black*). Panel *b* adapted with permission from Conan et al. (1995); copyright 1995 The Optical Society. Abbreviation: PID, proportional–integral–derivative.

In the case of read noise–limited short exposures, the SNR per exposure therefore increases with the exposure time $\propto \frac{D}{v}$. In practice, the gain is somewhere in between the above two regimes, i.e., $\propto D^{1/6...1}$. Although the sensitivity boost SNR $\propto D^{2...4}$ has already materialized with GRAVITY, it has not yet been able to take advantage of the increased coherence and fringe-tracking exposure times $\propto D^{1/6...1}$ because of excessive vibrations of large telescopes (Section 5.3).

5.2. Adaptive Optics

AO is the technique to correct the wave front distortion from Earth's turbulent atmosphere and to deliver diffraction-limited images for large telescopes. A wave front sensor measures the distorted wave front of a bright star, which is then compensated for in real-time with a deformable mirror (DM), so that also the image from nearby objects will be sharpened. The original concept goes back to Babcock (1953) and was followed up independently and in parallel in military and astronomical applications (Rousset et al. 1990). See, e.g., Beckers (1993) and Davies & Kasper (2012) for reviews of its history, principle, and applications in astronomy.

AO is also the prerequisite to efficiently interfere the light from telescopes with a diameter larger than the Fried parameter. Its decisive role was recognized already in the proposed implementation of the VLT interferometer (Merkle & Léna 1986, Beckers et al. 1990): While the sensitivity (SNR^2)—the faintest object detectable for a given observing time—of broadband interferometric observations scales only moderately $\propto D^{1/3}$ with the diameter D of large telescopes in the case of seeing-limited (so-called multispeckle) observations, the sensitivity increases $\propto D^4$ for diffraction-limited, single-mode interferometric observations. Therefore, dedicated AO was implemented from the very beginning in the 8-m UTs for VLTI (Arsenault et al. 2003) and later upgraded with the GRAVITY IR AO (Hippler et al. 2020). The Keck interferometer took advantage of the multipurpose Keck AO (Wizinowich et al. 2000). The smaller 1.8-m-diameter ESO ATs and the 1-m CHARA telescopes are now also equipped with AO (ten Brummelaar et al. 2012, Woillez et al. 2019).

Although the limiting magnitude of small telescope interferometers is set by fringe tracking, large telescope interferometers are limited by AO. The reason is that larger telescopes require ever higher-order AO, because each atmosphere turbulence cell has to be corrected independently, and therefore the AO-limiting magnitude is independent of the size of the telescope. Fringe tracking, however, only measures and stabilizes a single (average) phase irrespective of telescope size, and the limiting magnitude thus increases with telescope diameter D. Because of additional light losses between the AO at the telescopes and the fringe tracker in the interferometric laboratory, the limiting magnitude curves are shifted relative to each other, and the transition between the two regimes typically arises at 1–2-m telescope diameter as used in CHARA and the VLTI-ATs.

Laser guide star (LGS) AO overcomes this limitation (e.g., Beckers 1993, Davies & Kasper 2012). Here, the high-order wave front correction is done on an artificial star, created by a laser, and projected high up in the stratosphere. In this case, the limiting magnitude of the AO is set by the need for a tip–tilt reference star (two degrees of freedom per telescope), which is comparable with the fringe-tracking limit (one degree of freedom per telescope, but reduced optical throughput). A first demonstration of LGS AO-assisted interferometry was done at the Keck interferometer (Colavita et al. 2013) shortly before its shutdown. The GRAVITY+ project (Eisenhauer 2019) currently upgrades all VLT 8-m telescopes with LGSs and new AO (Section 7.2).

5.3. Fringe Tracking and Vibration Control for Minute-Long Exposures

Fringe tracking is the technique of tracking and correcting the phase delay between telescopes that is introduced by the turbulent atmosphere. Among the first to propose and later implement

active tracking and stabilization of the fringe position using a servo loop were Shao & Staelin (1977, 1980). A number of instruments followed the same path and implemented fringe tracking to allow the interferometric observation of faint sources by actively stabilizing on a nearby bright source (Colavita & Wizinowich 2003, Gai et al. 2003, Delplancke 2008, Kok et al. 2013).

The first element of a fringe tracker is the phase sensor, a beam combiner that measures the current fringe position (Section 4.2). A controller then compares the measured fringe position with a target position and commands an actuator (typically a fast piezo-mounted mirror) to correct the position. The different control-loop states (e.g., phase delay tracking close to the optical path zero, group delay tracking if the fringe is off by $>\lambda$, or fringe search in case the fringe has been lost) are handled by a state machine.

Vibrations from the telescopes, instruments, and infrastructure are an important limitation of fringe tracking. They excite the mirrors along the optical train and result in optical path length fluctuations with pronounced peaks at the frequencies of the excitation and at the mechanical resonance frequencies of the mirror and mounts. The detailed power spectrum (**Figure 12*b***) of the optical path variation is complex, with isolated peaks, forests of unresolved peaks, and a pseudocontinuum following a red power law.

At frequencies below a few hertz, the optical path fluctuations are completely dominated by vibrations, with an amplitude on the order of several to 10 μm. At the VLTI and LBTI, e.g., they are measured by accelerometers placed on the primary, secondary, and tertiary mirrors, and corrected by piezo-driven mirrors in the main delay lines in feed-forward open loop (e.g., Di Lieto et al. 2008, Böhm et al. 2017). After the bulk of these vibrations have been corrected, the turbulence of Earth's atmosphere dominates the optical path length fluctuations up to a few tens of hertz. This is the primary domain of the fringe tracker. At higher frequencies, the atmospheric perturbations have only little power, and on top, the averaging effect from large telescope aperture sets in (**Figure 12*a***), damping the high turbulence frequencies even more.

For large telescopes, however, this high-frequency range is again dominated by vibrations excited by, e.g., ventilators (around 48 Hz) and closed-cycle coolers of cryogenic instruments (around 80 Hz). The vibrations often come in the form of a forest of multiple, nearby frequencies, e.g., inductance motors with a slightly different frequency slip (typically of a few percent). With fringe-tracker frame rates of 100–500 Hz and corresponding closed-loop bandwidth of a few tens of hertz, most of these vibrations are beyond the control bandwidth. The vibrations are therefore corrected with predictive control, very much like in AO (e.g., Guesalaga et al. 2012, Kulcsár et al. 2012). One possible solution is to use phase-locked oscillators to track and correct a small number of vibration peaks (Di Lieto et al. 2008, Colavita et al. 2010). An alternative approach is to compensate the vibration spectrum and the atmospheric turbulence at the same time.

This can be achieved with a Kalman (1960) controller, a predictive algorithm whose commands are based on a model of the identified disturbance components. Menu et al. (2012) successfully ported the Kalman filtering to four-baseline fringe tracking, which was subsequently implemented in the GRAVITY fringe tracker by Choquet et al. (2014) and Lacour et al. (2019). The Kalman filtering outperforms the classical `PID` control, reducing the (vibration-driven) fringe-tracking residual error on the VLTI-UTs from 500–1,000 nm rms to ∼250 nm rms under typical conditions. On the small ATs, the fringe-tracking residuals reach <100 nm rms (Lacour et al. 2019). Only the successful compensation of the telescope vibrations enabled minute-long integration times in dual-field interferometry.

5.4. Dual-Beam Interferometry

Dual-beam interferometry refers to the simultaneous interferometric observation of two widely separated objects ($\theta \gg$ coherent field of view) contained inside the atmospheric turbulence

isopistonic patch (Section 3.3). The technique was first described by Shao & Colavita (1992) and later implemented by Colavita et al. (1999) at the PTI using star separators located at the focus of the telescope, which feed two independent beams to separate interferometric instruments. In the early 1990s, the interest in dual-field interferometry was primarily driven by the promise of high-precision astrometry (Section 6.1) and its application in the detection of exoplanets through the reflex motion of their host stars (in preparation for space astrometry missions for exoplanets). The possibility of fringe tracking on a bright object (Section 5.3) and of stabilizing and observing fringes of a much fainter nearby target was tentatively explored by Lane & Colavita (2003), but was not pushed beyond the limiting magnitude of the interferometer around $m_K = 5$ mag.

The dual-field instrument PRIMA (Phase Referenced Imaging and Micro-arcsec Astrometry; Delplancke 2008) was designed to equip the VLTI with astrometric and phase-referencing capabilities. The main science interest in exoplanet detection put an emphasis on astrometry rather than pushing the sensitivity of the interferometer. Delays in the project and competition from *Gaia* (Gaia Collab. et al. 2016) led to a stop of the astrometric efforts while the dual field capability of the infrastructure was briefly explored. The first dual-field phase-referenced observations, which reached a magnitude of $m_K = 12.5$ pushing the sensitivity by a factor of 10 compared to direct observations, were carried out by the ASTRA instrument on the Keck Interferometer (KI) (Woillez et al. 2014). The emerging scientific capability of the KI was stopped from flourishing by the shutdown of the facility in 2012. It took another 5 years to unlock the full potential of phase-referenced imaging and to push the sensitivity limits by a factor of 1,000 compared to direct detection. The GRAVITY instrument (GRAVITY Collab. et al. 2017a) routinely offers microarcsecond resolution imaging for objects fainter than $m_K = 19$ mag (Section 2.3).

5.5. Subelectron Read Noise Infrared Detector Arrays

Irrespective of detailed implementation, the tracking and compensation of atmospheric perturbations with AO or fringe tracking require exposure times shorter than the atmospheric coherence time. At typical frame rates of 1 kHz, i.e., exposure times of 1 ms, even bright objects are photon starved. This means that the performance of the sensor is limited by the readout noise of the detector (e.g., Finger et al. 2016). At the same time, the 1 kHz frame rate of typically a few thousand pixels requires a comparably high analog bandwidth on the order of a megahertz for reading the detector pixels.

The early IR fringe-tracking systems (e.g., PTI fringe tracker, FINITO at VLTI, FATCAT at Keck) used NICMOS3 (Near Infrared Camera and Multi-Object Spectrometer 3), PICNIC, or HAWAII arrays with typical readout noise for double-correlated sampling of $\approx$20–30e^- with exceptional systems reaching $\approx$5–10e^- (Colavita et al. 1999, Millan-Gabet et al. 1999, Vasisht et al. 2003). Although the IR detectors grew enormously in size from 0.065 Mpixel to 16 Mpixel over the past three decades, the improvements in terms of read noise have been marginal.

In order to overcome the CMOS (complementary metal-oxide semiconductor) noise barrier, ESO started in 2007 a program together with Selex ES (now LEONARDO) to develop HgCdTe-based electron avalanche photodiode (eAPD) arrays for the NIR (Finger et al. 2010). An independent eAPD development under the name "RAPID" was started by Sofradir, CEA-Leti, and a consortium of research institutes (Feautrier et al. 2014). HgCdTe is a well-suited detector material for avalanche multiplication because the mass of the electron is much smaller than the mass of the holes and the APD process results in pure electron multiplication. HgCdTe is a direct semiconductor; i.e., electron–hole pairs are created without phonon interaction. This means that large avalanche gains with almost no excess noise are possible with HgCdTe-based APDs (Finger et al. 2016). After several development cycles of solid state engineering, the eAPD

arrays have matured and resulted in the 320 × 256-pixel SAPHIRA (Selex Advanced Photodiode HgCdTe Infrared Array) arrays. The first units were implemented in the GRAVITY fringe tracker and Coudé Infrared AO units (CIAO). At short integration times (∼1 ms) the SAPHIRA arrays achieve subelectron noise ($<0.2e^-$), high APD gain (up to 700), and an excess noise of only ≈1.3 (Finger et al. 2016, 2017). The introduction of the SAPHIRA arrays in AO and interferometry and the corresponding noise reduction from $\sim 10e^-$ to $<1e^-$ has been revolutionary and has played a considerable role in the success of VLTI/GRAVITY. A number of interferometer and AO facilities at observatories (e.g., Keck, Subaru, Kitt Peak, CHARA, and Palomar) also adopted the SAPHIRA (e.g., Goebel et al. 2018).

The latest detector generation Mark14, grown by metal organic vapor phase epitaxy (MOVPE), has extended the sensitivity range to 0.8–2.5 μm (Finger et al. 2016). Current developments include high-speed 512 × 512-pixel eAPD arrays for AO applications on 30–40-m telescopes (Finger et al. 2019, 2022) and large format science detectors (Claveau et al. 2022, Feautrier et al. 2022).

5.6. Breakthrough in Sensitivity: Summary Points

1. Sensitivity of O/IR interferometers scales with high powers of telescope size.
2. AO, vibration control, and fringe tracking allow for minute-long exposures—by a factor of 1,000 longer than the atmospheric coherence time.
3. Dual-beam interferometry enables routine milliarcsecond resolution imaging of objects fainter than 19 magnitude.
4. eAPD detectors revolutionized the field of AO and interferometry.

6. PRECISION INTERFEROMETRY

6.1. Narrow-Angle Astrometry

Ground-based astrometry is fundamentally limited by Earth's atmosphere. This limitation manifests itself in scintillation, image blurring, and image motion in the case of single-dish imaging. In the case of multiple apertures, astrometry is limited by the fringe jitter introduced by the atmospheric turbulence. The jitter of two stars, however, is correlated, depending on their separation and the aperture size (or baseline in the case of an interferometer). With narrow-angle astrometry, we denote the regime when the angular separation between two sources is small enough that their beams experience essentially the same atmospheric perturbations.

This narrow-angle regime is defined by Shao & Colavita (1992) as the angular separation $\theta \ll B/h$, with the baseline B and the effective turbulence height h. Among the first to recognize the potential of narrow-angle astrometry was Lindegren (1980). The application in interferometry was later proposed by Shao & Colavita (1992). They realized the possibility of microarcsecond astrometry with long-baseline interferometry. Using SCIDAR (SCIntillation Detection and Ranging) measurements of the atmospheric turbulence height profile at Mauna Kea, Shao & Colavita (1992) derived an expression of the differential astrometric error for $\theta \ll B/3{,}000$ m. The residual error behaves as $\sigma \approx 1.45 \times 10^{-3}\, B^{-2/3}\, \theta\, t^{-1/2}$ arcsec, with the source separation θ in arcseconds and the integration time t in seconds. Of particular importance in the narrow angle regime is the $\sigma \propto B^{-2/3}$ dependence, which explains why large interferometer arrays are key to high-precision astrometry. Assuming a baseline of 100 m and a separation of 2 arcsec, the residual atmospheric error averages to ∼10 μas within 5 min of integration time.

The principle of differential astrometry between two objects on sky relies on the measurement of the optical path difference ΔOPD of the two objects, which originates from the geometric delay introduced by the different projection of the baseline **B**. The basic astrometric equation

$\Delta\mathrm{OPD} = \mathbf{B} \times \mathbf{s} + \Delta\mathrm{OPD}_{\mathrm{int}}$ relates the measured ΔOPD between the two objects, their differential optical path inside the interferometer $\Delta\mathrm{OPD}_{\mathrm{int}}$ and the object separation $\mathbf{s} = (\alpha - \beta)$, where α and β are the positions of the two objects. A simple sensitivity analysis illustrates the required accuracies: $\delta s = \frac{\delta B}{B} \times s + \frac{\delta \Delta\mathrm{OPD}}{B}$. Let's assume the desired astrometric accuracy is 10 μas, the baseline is $B = 100$ m, and the source separation is $s = 1$ arcsec: This means that the baseline needs to be calibrated to millimeter accuracy, and the combined optical path delay error must be measured accurately to within a few nanometers. The astrometric equation becomes significantly more complex when systematic uncertainties due to the residual atmosphere, baseline calibration, instrument and telescope alignment as well as metrology, polarization and dispersion errors are considered. The following list gives an overview of major astrometric error sources: (*a*) Baseline errors originate from the difficulty of measuring and calibrating the B_{NAB}, which is physically realized by the end points of the metrology (Section 6.2). Depending on the location of the end points, $\mathbf{B}_{\mathrm{NAB}}$ can be impacted by differential telescope flexure or runout. (*b*) OPD errors ($\Delta\mathrm{OPD}_{\mathrm{S}} = \phi_{FT} \times \frac{\lambda_{FT}}{2\pi} - \phi_{SC} \times \frac{\lambda_{SC}}{2\pi}$) introduced by phase measurement and wavelength calibration errors in the fringe tracking or science channel. (*c*) Metrology errors ($\mathrm{OPD}_M = \phi_M \times \frac{\lambda_M}{2\pi}$), here most importantly the wavelength, because the metrology traces differential OPDs on the order of a few 10s to 100s of millimeters. (*d*) Dispersion errors $\Delta L_{\mathrm{fib,air}}(\frac{n_{\mathrm{fib,air}}(M)}{n_{\mathrm{fib,air}}(S)} - 1)$ from inaccurate calibration of the different refractive index between the metrology and the science wavelength in air or glass. (*e*) Pupil misregistration of the science and metrology beams in combination with pointing errors. They lead to phase errors of the order $\Delta\boldsymbol{\alpha} \times (\mathbf{P}_{\mathrm{S}} - \mathbf{P}_{\mathrm{M}})$. (*f*) Polarization-induced astrometric errors from differential birefringence in the interferometer arms. Because the metrology laser is linearly polarized, birefringence can introduce an effective path difference between the laser and the unpolarized science objects.

These and more astrometric errors have been studied by Colavita (2009) and Woillez & Lacour (2013) as well as in particular for the GRAVITY instrument by Lacour et al. (2014a,b). The impact of polarization has been studied by Lazareff et al. (2014).

6.2. Interferometric Baselines Revised

For infinitely small telescopes, the interferometric baseline is the separation vector between the apertures. It gives the optical path difference between the two telescopes when observing a point-like object (Section 3.1), sets the spatial frequency in interferometric imaging and the van Cittert–Zernike relation (Section 3.2), and results in the ΔOPD between two neighboring objects in phase-reference observations (Section 5.3). For large telescopes, however, the baselines for the three cases are not identical, and each of them follows a different physical realization. The effects are often nonintuitive, especially for narrow-angle astrometry (see **Figure 13**; Section 6.1). Woillez & Lacour (2013) and Lacour et al. (2014a) concisely reviewed the three concepts in preparation for the GRAVITY instrument, building on the learning from the earlier ASTRA (Woillez et al. 2010) and PRIMA (Delplancke 2008) experiments.

The wide-angle baseline is the separation between the pivot points of the telescopes. Because each telescope points toward the object, there is no phase gradient across the aperture, and all light rays have the same optical path length irrespective of their pupil position. The wide-angle baseline tells where to preset the delay lines to find the fringes and, when precisely known, allows for measuring the absolute position of the star on the celestial sphere. The wide-angle baseline is calibrated from stars with known coordinates, and for precision wide-angle astrometry, the position of the telescopes pivot points are measured and monitored with dedicated laser metrology, e.g., at NPOI (Armstrong et al. 1998).

The imaging baseline sets the spatial frequency sampled by the interferometer. The observed complex visibility is then the Fourier transform of the object's intensity distribution (Section 3.2).

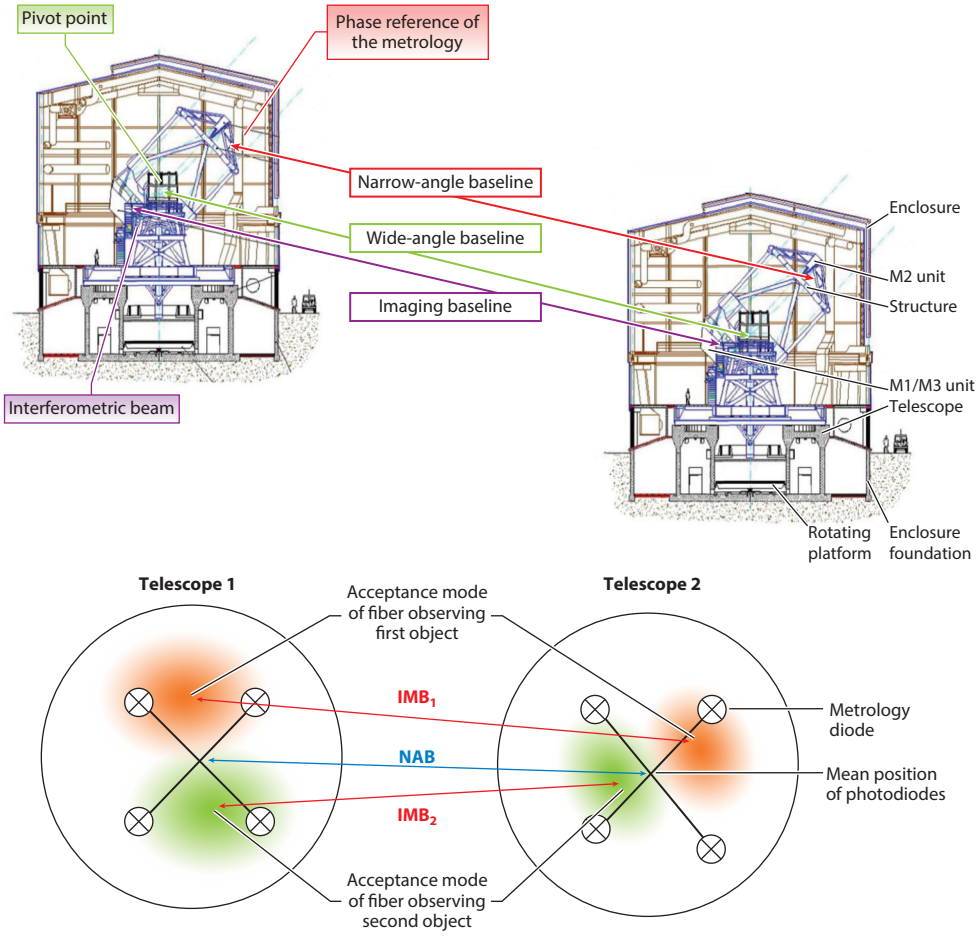

Figure 13

Baselines in O/IR interferometry. The separation between the telescopes of an interferometer is called the baseline. In detail, we distinguish three types, each of them with a specific property and physical realization: The WAB obeys the delay equation and is realized by the pivot points of the telescopes. The IMB sets the spatial frequency in interferometric imaging and is realized by the entrance pupil weighted by the Gaussian beam of the instrument single-mode fibers. For a dual-beam interferometer, the IMBs can be different for the two objects because of optical misalignment. The NAB is the separation between the end points of the metrology system, which measures the internal path difference between two objects. Figure adapted from Lacour et al. (2014a). Abbreviations: IMB, imaging baseline; NAB, narrow-angle baseline; WAB, wide-angle baseline.

The imaging baseline is given by the autocorrelation of the telescopes apertures as seen from the object (Thompson et al. 2017). More accurately, it includes the coupling of the electric field probed by the beam combiner instrument—i.e., the Gaussian mode of the instrument's single-mode fiber—and the beam relay from the telescope to the beam combiner.

Finally, the narrow-angle baseline links the distance of the interferograms of two separated objects, each measured with its own beam combiner. The differential optical path between the two interferograms is measured by laser metrology, probing the path length from each beam combiner to the telescopes (Section 6.1). More accurately, the narrow-angle baseline is the

separation between the end points of the laser metrology, where the path length difference is measured, again, as seen from the object. The metrology end points for narrow-angle astrometry are best placed in front of the telescope, e.g., for GRAVITY on the spider holding the secondary mirror (Lippa et al. 2016), because even small wobbles from the optical relay would alter the apparent position of internal end points and thereby corrupt the narrow-angle astrometry.

6.3. Laser Metrology in Interferometers

A key component of any dual-beam interferometer is a dedicated metrology system, which provides an optical link of the two beam combiners and their science interferograms. The metrology monitors the internal path length with nanometer accuracy to enable high-precision astrometry. In some cases, the system also serves as a feedback for differential delay lines, which compensate for the OPD of the two objects (here referred to as *FT* and *SC*). As discussed in Section 6.2, the end points of the metrology, i.e., the points to which the internal optical paths are measured, define the narrow-angle baseline $\mathbf{B}_{\mathrm{NAB}}$ of the interferometer. Several metrology concepts have been developed for dual-field interferometers. The metrology systems implemented in PTI (Colavita et al. 1999) and PRIMA (Leveque et al. 2003) rely on two heterodyne Michelson interferometers, which measure for each object the optical path change between the telescopes. The internal path difference between the objects, $\Delta\mathrm{OPD}_{\mathrm{int}}$, corresponds to the difference between the path variations recorded by the two heterodyne interferometers.

The PRIMA metrology launches the lasers at the center of the pupil plane close to the beam combiners, and they are retroreflected at the telescopes. The internal path difference $\Delta\mathrm{OPD}_{\mathrm{int}} = (T1 - T2)_{FT} - (T1 - T2)_{SC}$, i.e., the difference between the path variations, is recorded by photodiodes. The signal is filtered, and the individual heterodyne signals are mixed such that the disturbance to be monitored is directly coded in the phase of the carrier signal. The GRAVITY metrology (Lippa et al. 2016) splits the laser light into three beams with fixed phase relations. Two of the beams are faint and injected backward into the two beam combiner chips. The third, high-power beam is overlaid on top of the two faint ones after they have passed the fibers within the instrument and acts as a phase-preserving amplifier for the detection. This approach minimizes the inelastic scattering of the metrology light in the instrument fibers. At each telescope, the three beams interfere in the pupil plane and form a fringe pattern. By temporal phase modulation of the two faint beams at different kilohertz frequencies, the phase signal of the two light paths can be extracted using lock-in amplifiers. The metrology measures the path variation between the objects to a single telescope. The difference of the variation between two telescopes provides the desired internal $\Delta\mathrm{OPD}_{\mathrm{int}} = (FT - SC)_{T1} - (FT - SC)_{T2}$ between the two objects.

A subtle but important distinction between the two metrology concepts originates from the way the $\Delta\mathrm{OPD}_{\mathrm{int}}$ is measured. The PRIMA-like design allows for measuring and correcting vibrations occurring between the telescopes. However, a serious caveat of the PRIMA concept is that the metrology cannot trace the beam before the AO DM, because it would imprint its deformation in the $(T1 - T2)$ path, thereby folding the atmospheric perturbations to the metrology signal. As a consequence, the metrology end points need to be downstream of the DM far away from the telescope primary mirror, which penalizes the B_{NAB} stability. In the GRAVITY concept, the two laser beams $(FT - SC)$ go through the same DM; i.e., the difference signal does not see the deformation, which allows extending the metrology up to the telescope pupil, a decisive advantage for the stability of B_{NAB}. This comes at the cost that vibrations impacting the fringe tracker and science beam are not traced by the metrology.

Both metrology concepts rely on frequency stabilized lasers, which operate at wavelengths shorter than the science band to minimize stray light. In both cases, the laser frequency $\nu = c/\lambda$ needs to be sufficiently stable such that the corresponding OPD error is less than 1 nm over a

differential internal OPD of a few hundred millimeters. This corresponds to a frequency stability of better than 10^{-8}.

6.4. Field and Pupil Stabilization

The use of single-mode fibers mandates the accurate control of the star's position to better than the diffraction limit. This is typically achieved by a combination of AO (Section 5.2) and/or guider at the telescope, and a lab- or instrument-provided secondary guiding on the object itself to correct the image motion from imperfect beam relay. This two-stage approach provides the large field of view at the telescope for picking a bright, nearby star for telescope guiding, so that the secondary guider can run with longer exposure times and accordingly higher sensitivity. The lab guider (e.g., Gitton et al. 2004, Crawford et al. 2006) is typically a dedicated camera, operating at a different wavelength and serving several instruments. This comes with the disadvantage of noncommon guiding errors, e.g., from atmospheric refraction. The field stabilization requirements are especially hard for narrow-angle astrometry (Section 6.1), for which even small tilt errors (on the order of 10 mas) reduce the astrometric accuracy through cross terms with pupil errors. In this case, the guiding is directly done on the fiber by slightly (radius of a few milliarcseconds) modulating the tip–tilt at high frequency (a few tens of hertz) and using the correlation between the measured flux and modulation signal (in analogy to a lock-in amplifier) as feedback to the control loop (e.g., Bonnet et al. 2006). Some beam combiner instruments also provide internal wave front sensors (Anugu et al. 2018) for secondary guiding of low-order aberrations, in particular focus.

It is also the narrow-angle astrometry that requires accurate pupil control, typically to well below a percent of the telescope diameter. Because of the difficulty to see and track the pupil on faint objects, pupil guiding is implemented by means of laser beacons, taking advantage of either the path length metrology (e.g., Woillez et al. 2014) or dedicated laser beacons launched from the spider arms holding the telescope's secondary mirror (Anugu et al. 2018). Most interferometers do not reimage the telescope pupil but transfer only a collimated beam to beam combiner instruments, and therefore they have zero field of view. The VLTI is the only interferometer with variable curvature mirrors (Ferrari et al. 2003) in the retroreflectors of its delay lines to dynamically transfer the telescope pupil and to provide a coherent field of view of 2–6 arcsec for the beam combiner. As the delay lines move to compensate the path length difference between the telescopes, the curvature of this mirror is adjusted either blindly or in closed loop on the laser beacons launched at the telescope (Anugu et al. 2018).

6.5. The Role of Optical Aberrations in Interferometry

The introduction and implementation of single-mode fibers (Froehly 1981, Shaklan & Roddier 1987, Coudé du Foresto et al. 1998) and resulting improvements in the calibration were breakthroughs in O/IR interferometry. The spatial filtering from single-mode fibers converts phase errors across the telescope pupils in amplitude fluctuations, which can be monitored and then corrected in the calculation of the visibility (Section 4.2). It thus removes the random phase fluctuations of the turbulent atmosphere as the dominant calibration error (e.g., Perrin et al. 1998, for a first demonstration). Dynamic aberrations like atmospheric tip–tilt result in an increased field of view (Perrin & Woillez 2019). Static optical aberrations have a more subtle effect on the interferometric measurement. The phase of the electric field from a point source is then not constant anymore across the Airy peak of the telescope point spread function but is a function of the position within the field of view.

In radio interferometry, the effect is known as direction-dependent (complex) gains (Bhatnagar et al. 2008). For O/IR interferometry, it was for the first time described and corrected

by GRAVITY Collab. et al. (2021b). Even for diffraction-limited optics the static aberrations are on the order of $\lambda/10$, translating to comparable signatures in the interferometric measurements, or when expressed in position errors on sky, 1/10 the interferometric beam size for objects located at the edge of the interferometer's field of view. In GRAVITY, e.g., the calibration of the field-dependent phase errors is done by scanning the field of view with the instrument internal calibration unit. The correction is then applied via a modified van Cittert–Zernike theorem in the forward modeling as part of the model fitting (e.g., when fitting the measured visibilities and closure phases with a binary star) or image reconstruction (GRAVITY Collab. et al. 2022a).

6.6. Nulling

Perhaps the technique with potential to deliver the most extreme precision is nulling interferometry, with a goal of $\ll 10^6$ contrast to detect Earth-like planets in the MIR. Akin to phase-mask coronagraphy on single apertures (see, e.g., the review by Mawet et al. 2012), nulling uses destructive interference to remove host-star light while allowing light from a faint nearby object to be detected. Nulling interferometry potentially has the combination of angular resolution and high contrast to characterize a large number of Earth-like planets around other stars, especially in the thermal IR, where many molecular biomarkers can be seen in the planetary atmospheres (e.g., Quanz et al. 2022).

The principle behind nulling was laid out by Bracewell (1978) and Angel & Woolf (1997): If one interferes light from two telescopes onto a beam splitter with a π relative phase shift, then the electric fields destructively interfere and one beam splitter output is completely dark, except for the light from a second object (e.g., an exoplanet) slightly offset on the sky. In practice though, there are many difficulties, including chromaticity of phase delay, electric field amplitude and polarization matching, wave front aberrations, stellar diameter leakage, and fringe-tracking stability. The first sky nulling was performed by Hinz et al. (1998) using subapertures from a single telescope, where a π phase shift was created using glass combinations and achieved $\approx$4% null depths at best in open loop. Long-baseline nulling at the Keck Interferometer (Serabyn et al. 2012, using a field inversion for nulling) and the LBTI measured the exozodiacal dust contributions around nearby stars: Colavita et al. (2009) reported raw null depths of 1.5–2% in the IR and Defrère et al. (2016) also achieved $\approx$1% raw null depths at the LBTI. While only achieving raw null depth on the order of 1%, nulling interferometers have reached a calibrated nulling accuracy after post-processing below 0.05% at both *K* band (defined as 2.0–2.4 μm; Mennesson et al. 2011) and *N* band (defined as 7.5–14.5 μm; Defrère et al. 2016). These surveys (described by Millan-Gabet et al. 2011, Defrère et al. 2016) concluded that exozodiacal dust is generally not large enough to interfere with future exoplanet searches (Mennesson et al. 2014, Ertel et al. 2020). Due to the importance for nulling to the future of exoplanet studies, theoretical and experimental work remains active. We point the reader to recent explorations of the optimal nulling architectures (e.g., Guyon et al. 2013, Hansen et al. 2022), ways to combine nulling with closure phases (Lacour et al. 2014b), nulling within IO (e.g., Hsiao et al. 2010, Errmann et al. 2015, Martinod et al. 2021), and development of better IR-friendly materials for IO, such as lithium niobate (Hsiao et al. 2009) and chalcogenides (Kenchington Goldsmith et al. 2017). There is a new exoplanet-focused instrument, VLTI/NOTT (Nulling Observations of exoplaneTs and dusT; Defrère et al. 2018), under construction that will push nulling down to the *L* band (3.8 μm) for the first time, and there is an active consortium proposing a space-nulling interferometer, the Large Interferometer for Exoplanets (LIFE; Quanz et al. 2022). More discussion of nascent space interferometer efforts is in Section 7.5. Space is indeed the place for nulling because ground-based interferometry is tragically limited by atmospheric turbulence and thermal emission that degrade the achievable contrast far from fundamental limits.

6.7. Precision Interferometry: Summary Points

1. Interferometers provide much more accurate astrometry than single telescopes.
2. It is necessary to distinguish among three kinds of baselines: wide-angle baseline, imaging baseline, and narrow-angle astrometry baseline.
3. Laser metrology measures path length differences to nanometer accuracy.
4. Active field and pupil control are key to canceling second-order astrometric error terms.
5. Aberrations introduce phase variations across the field of view and limit the astrometric and imaging accuracy, but they can be corrected by forward modeling.
6. Nulling is the interferometry equivalent to coronagraphy to block out the starlight.

7. FUTURE DIRECTIONS

So far we have concentrated our discussion of the breakthrough in sensitivity on the gain from large telescopes, AO, fringe tracking, and dual-beam interferometry. But where do we stand in comparison to fundamental limits, i.e., quantum noise and background noise? How much more can we gain, and which directions should we go?

7.1. Far from Fundamental Limits

The quantum limit for the measurement of the phase from a two-telescope interference is given by the Heisenberg uncertainty principle $\Delta\phi\Delta N < \frac{1}{2}$, where $\Delta N = \sqrt{N}$ is the uncertainty in the number of photons N in the measurement (e.g., Townes 2000). The resulting SNR of the fringe contrast in the photon noise limit is given by $\mathrm{SNR} = V\sqrt{N}$. The number of photons needed to detect fringes (SNR = 5) from a partially resolved object ($V = 0.5$) is ≈100 photons, which for the case of two 8-m-diameter telescopes and observing at K band translates to 31 mag for a one-hour exposure. This is about 100,000 times fainter than currently reached with GRAVITY. How far are we from the atmospheric and thermal background limit? In this case, the noise is dominated by the background, and the SNR of the fringe detection is $\mathrm{SNR} = V\frac{N}{\sqrt{N+B}} \approx V\frac{N}{\sqrt{B}}$, where B is the number of background photons. For a single-mode instrument operating at the diffraction limit, the atmospheric background at K band is $\approx 10^3$ photons s^{-1}. The thermal emission from a black body with the average temperature of the laboratory of 16°C translates to $\approx 10^4$ photons s^{-1}, which is roughly a factor of 10 more than the atmospheric background. The number of photons needed for the detection of a partially resolved object in one hour is then approximately a few 10^4, corresponding to ≈25 mag, or a factor of a few hundred fainter than currently possible.

7.2. Enhancing Sensitivity

Why are current O/IR interferometers falling several orders of magnitudes behind the fundamental limit? The reason is a combination of low throughput, detector noise, instrumental background, and coherence loss. Here, we illustrate the situation using the example of GRAVITY, and we sketch out possible improvements from the ongoing upgrade to GRAVITY+ (Eisenhauer 2019).

The worst offender is throughput: The total detected quantum efficiency (QE) is ≈0.1–1%. The losses are dominated by AO performance (having a Strehl ratio of typically 10–40%), the beamtrain from telescopes to instrument (throughput $T \approx 35\%$), IO ($T \approx 54\%$), and traditional optics losses (e.g., grism efficiency ≈25–50%). On top of this there is a factor of 2 loss from splitting the light between fringe tracker and science beam combiner, and a factor of 3 from the pairwise combination of the 4T array. Some losses can be reduced with current technology: Taken together, better LGS AO, improvements in traditional optics, and going to dual-beam interferometry will bring a factor of 10–20 better throughput, thereby increasing the detective QE up

to ≈10%. The losses from the pairwise beam combination remains a fundamental issue, because there is no noise-free amplification at O/IR wavelengths. Focal plane beam combination (e.g., the so-called hypertelescope; Labeyrie 1996) can partly overcome this limitation, but it faces practical limitations from detector noise and difficult calibration.

The second worst offender is noise: For minute-long exposures, GRAVITY observations are limited by the laser background from the metrology. Reducing the laser power or the interleaved operation will bring the laser background to below the detector noise, improving the sensitivity by a factor of 1.5–5. At that stage, zero-noise eAPD detectors (Section 5.5) can again revolutionize sensitivity. Their long-exposure noise is currently dominated by a high dark current, but revised diode structures, readout circuits, and optimized operation have already led to a demonstration of dark current $0.025e^-$ s^{-1} pix^{-1} (Atkinson et al. 2018) and read noise $\lesssim 3e^-$ in minute long exposures (Finger et al. 2019, 2022). Also, large-format eAPD detectors are in the making (Claveau et al. 2022, Feautrier et al. 2022). These detectors are then expected to reduce the noise of high spectral resolution observations by another factor of 2–10.

The last offender is coherence loss: While polarization mismatch between telescopes is typically well corrected, fringe-tracking residuals are catastrophic (≳500 nm with frequent fringe losses) for observations at the sensitivity limit, when the fringe tracker control bandwidth is reduced. For large telescopes, the coherence loss is then dominated by high-frequency telescope vibrations (Section 5.3). Expanding accelerometers to the full Coudé optical train (Bigioli et al. 2022), together with further reducing the source of vibrations (Woillez et al. 2018), should allow for 100-nm fringe tracking also for 8-m telescopes (e.g., for exoplanet work), as well as increase the coherence at the current sensitivity limit by a factor of 2 (e.g., extragalactic objects).

All together, higher throughput, reduced instrument background, zero-noise detectors, and better vibration control will enhance the sensitivity of current interferometers by another 1–2 orders of magnitude, with a limiting magnitude then beyond $m_K \approx 22$ mag.

7.3. Enhancing Sky Coverage

GRAVITY's leaps in sensitivity by factors of thousands resulted from dual-beam interferometry and fringe tracking on a nearby reference star. Because it splits the light of the two objects in the instrument, the maximum separation is 2 arcsec for the UTs. GRAVITY Wide (GRAVITY Collab. et al. 2022c) has extended its dual-beam capability to also take advantage of the previously installed PRIMA dual-beam infrastructure. The maximum separation between the two objects can then be up to several tens of arcseconds, limited only by Earth's turbulent atmosphere. The limit is set by the isopistonic angle θ_P, at which the phase between the two objects becomes uncorrelated.

The sky coverage is ultimately given by the combination of the isopistonic angle and the limiting magnitude for fringe tracking. Both increase with telescope diameter, and we show below that the advantage of large telescopes for dual-beam interferometry even exceeds the SNR advantage outlined in Section 5.1. First, the isopistonic angle increases with telescope diameter $\theta_P \propto D^{1/6}(\text{const.} + D)$ (Elhalkouj et al. 2008, Boskri et al. 2021), because in this case the beams from the two stars partially overlap and, thereby, see the same atmospheric perturbations (**Figure 12**). As a result, the isopistonic area for off-axis interferometry around a fringe-tracking star increases $\propto D^{1/3\ldots7/3}$. For typical atmospheric conditions, the isopistonic angle increases from ≈12 arcsec to ≈50 arcsec when going from 1-m to 10-m telescopes. Second, the gain in SNR $\propto D^2$ and the reduced bandwidth requirement for fringe tracking $\propto D^{1/6\ldots1}$ relax the brightness requirement by a factor $\propto D^{2.2\ldots3}$, which for a star luminosity function N (stars brighter given flux S) $\propto S^{-3/2}$ increases the sky density of suitable stars $\propto D^{3.3\ldots4.5}$.

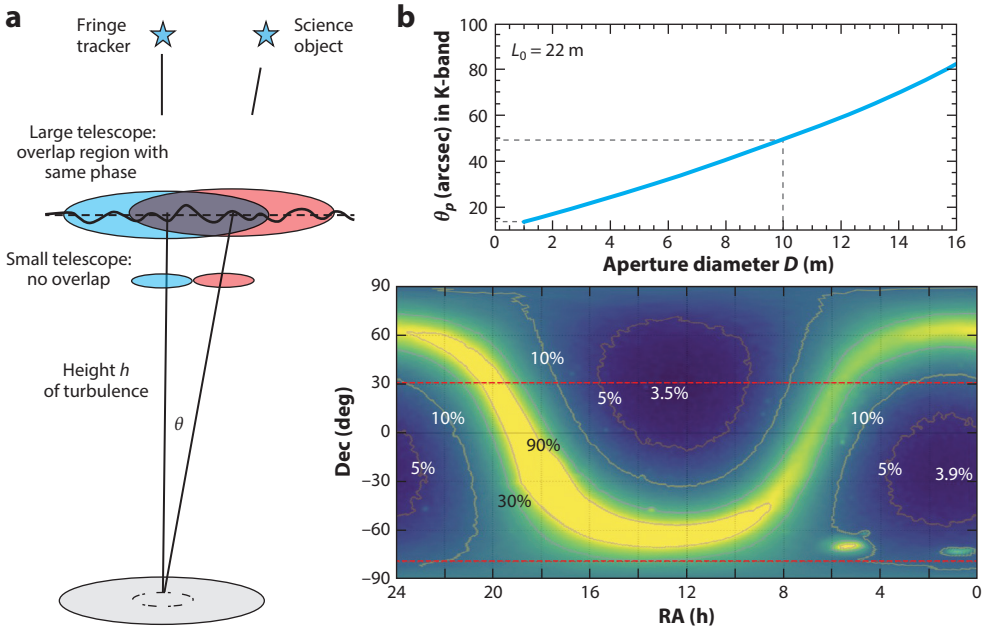

Figure 14

Enhanced sky coverage for large telescopes. (*a*) When observing two objects simultaneously, the two beams overlap for large telescopes, thereby increasing the isopistonic angle with telescope diameter (*b*; modeled on Elhalkouj et al. 2008). (*c*) The resulting sky coverage for 8-m telescopes with a fringe-tracking limiting magnitude, $m_K = 13$ mag.

Taken together, the larger isopistonic area and the access to fainter fringe-tracking stars increases the sky coverage for dual-beam interferometry $\propto D^{3.6\ldots6.8}$. Vibrations and imperfect AO will eat up some of the advantages of large apertures, but it is only the 10-m-class telescopes, in combination with LGS AO, that will provide full (in the galactic plane) and substantial (for extragalactic observations outside the galactic plane) sky-coverage for off-axis fringe tracking (**Figure 14**).

7.4. Enhancing Wavelength and Baseline Dynamic Ranges

The wavelength range covered by O/IR interferometry is continuing to grow. MATISSE (Lopez et al. 2022) extended VLTI imaging capabilities to observe the *L*, *M*, and *N* bands (3–12 μm) simultaneously with four telescopes. Using the GRAVITY fringe tracker will push limiting magnitudes especially for observations with higher spectral resolution, although only a few results are out as of this date. VLTI will also stretch to shorter wavelengths with the *J*-band BIFROST instrument, which is under construction (Kraus et al. 2022). Visible imaging with 0.3-mas angular resolution should now be possible at NPOI and CHARA, and we expect results in the near future for dwarf stars, interacting binaries, gaseous disks, and stellar surfaces. Visible imaging will be boosted as NPOI integrates new 1-m telescopes with AO into the system. Improved imaging needs better UV coverage, and this means adding telescopes and baselines. Although harder, there is progress here too as CHARA is adding a seventh mobile telescope that will be connected to the array with single-mode fibers, leading to potentially longer baselines as well as more dense UV coverage. Ultimately, new facilities are needed to make a breakthrough in imaging and the MROI hopes to do this with ten movable telescopes. Although MROI will not have substantially

longer baselines than CHARA, the UV plane will be radically better sampled with virtually no gaps in the UV plane, making high-fidelity imaging truly possible. This project is partially funded with first fringes expected in 2023. The PFI project (PFI; Monnier et al. 2018) explored the science potential of a 12 × 3-m array with 1.2-km baselines and found an exciting science case for detecting giant exoplanets as they are forming in young disks using *K*- and *L*-band nulling, but also concluded that sensitivity was insufficient to go below a few Jupiter masses. As the SNR for observations of point sources scale as $\sqrt{N_{\rm tel}}D^2$ in the background limit (Section 5.1), truly revolutionary capabilities await ground-based arrays of ten or more 8-m-class telescopes (i.e., a scaled up VLTI-UT) rather than many small telescopes—or a move to space, where the IR background is smaller by millions or even billions.

Formation flying: maintaining relative separation and orientation between multiple spacecrafts; prerequisite for large baseline interferometry in space

7.5. Space Interferometry

O/IR interferometry is well suited to space, as all the major difficulties from the ground are missing: atmospheric turbulence that limits coherent integration times, light losses from complex optics to transport and delay light as stars move across the sky, and severe thermal IR backgrounds. The first attempts in the 1990s and 2000s to build space interferometers were ultimately not pursued, namely the *Space Interferometer Mission* (SIM; aimed at precision astrometry) and two MIR nulling interferometers—*Darwin* (from the European Space Agency) and the *Terrestrial Planet Finder Interferometer* (TPFI)—designed to detect and characterize Earth-like planets. A new flagship mission called LIFE, the Large Interferometer for Exoplanets (e.g., Quanz et al. 2022), is being proposed. The nulling interferometer with 4 × 2-m telescopes working in the thermal-IR aims at detecting 550 exoplanets, with 25–45 being rocky planets in their habitable zones. For 3.5-m telescopes, the last number jumps to 60–80 planets that might harbor life. Recent technical advances make space interferometry more feasible, including successful formation-flying missions [e.g., GRACE-FO (*Gravity Recovery and Climate Experiment Follow-On*), LISA (*Laser Interferometer Space Antenna*) Pathfinder], lower launch costs, and the maturation of cubeSats and commercial smallSats (see detailed overview by Monnier et al. 2019). The first space interferometer SunRISE (*Sun Radio Interferometer Space Experiment*) (6 cubeSats in radio; Kasper et al. 2019) will be launched in ∼2024, and multiple optical designs using smallSats have been proposed (e.g., Matsuo et al. 2022). Although the near-term political and technical outlook is still uncertain, the scientific potential of space nulling interferometry to measure the MIR spectra of Earth-like planets is still highly compelling and recognized as one of the most important long-term goals for astronomy.

7.6. Future Directions: Summary Points

1. Current interferometers fall many orders of magnitude behind fundamental limits.
2. Worst offenders of being behind limits are adaptive optics performance (AO), optical throughput, metrology laser background, detector noise, and vibrations.
3. The ongoing GRAVITY+ upgrade with laser guide star (LGS) AO and wide-field dual-beam capability will boost sky coverage by orders of magnitude.
4. Current facilities continue to expand instrumentation to wider wavelength ranges and offer a test bed for new technologies, such as nulling.
5. VLTI and CHARA will remain unique in the era of upcoming 30–40 m extremely large telescopes (ELTs), not for sensitivity but for angular resolution.
6. New ground- and space-based interferometers are under construction (e.g., MROI) or proposed (e.g., PFI, LIFE).
7. Technologies to pursue include affordable 8-m telescopes, interferometric LGSs, formation-flying space interferometry, and photon-counting IR detectors.

DISCLOSURE STATEMENT

The authors are not aware of any affiliations, memberships, funding, or financial holdings that might be perceived as affecting the objectivity of this review.

ACKNOWLEDGMENTS

We thank all our colleagues for inputs, discussions, comments, and corrections, in particular Mark Colavita and Julien Woillez on the technical advances, and Stefan Gillessen, Sylvestre Lacour, Karine Perraut, Guy Perrin, and Taro Shimizu on the astrophysical breakthroughs. J.D.M. thanks Fabien Baron for his contributions to the interferometric imaging. F.E. and O.P. are grateful to Reinhard Genzel, Tim de Zeeuw, and Dieter Lutz for many valuable inputs throughout the preparation of this manuscript. We thank our editor, Joss Bland-Hawthorn, for his feedback and guidance in preparing the review.

LITERATURE CITED

Akeson RL, Boden AF, Monnier JD, et al. 2005. *Ap. J.* 635(2):1173–81
Alexander T. 2005. *Phys. Rep.* 419(2–3):65–142
Amorim A, Bauböck M, Berger JP, et al. 2019. *Phys. Rev. Lett.* 122(10):101102
Andrews SM, Huang J, Pérez LM, et al. 2018. *Ap. J. Lett.* 869(2):L41
Angel JRP, Woolf NJ. 1997. *Ap. J.* 475:373–79
Antonucci RRJ, Miller JS. 1985. *Ap. J.* 297:621–32
Anugu N, Amorim A, Gordo P, et al. 2018. *MNRAS* 476:459–69
Anugu N, Le Bouquin JB, Monnier JD, et al. 2020. *Astron. J.* 160(4):158
Armstrong JT, Mozurkewich D, Rickard LJ, et al. 1998. *Ap. J.* 496:550–71
Arsenault R, Alonso J, Bonnet H, et al. 2003. *Proc. SPIE Conf. Ser.* 4839:174–85
Atkinson D, Hall D, Goebel S, et al. 2018. *Proc. SPIE Conf. Ser.* 10709:107091H
Babcock HW. 1953. *Publ. Astron. Soc. Pac.* 65(386):229–36
Baldwin JE, Beckett MG, Boysen RC, et al. 1996. *Astron. Astrophys.* 306:L13–16
Baldwin JE, Boysen RC, Cox GC, et al. 1994. *Proc. SPIE Conf. Ser.* 2200:118–28
Balick B, Brown RL. 1974. *Ap. J.* 194:265–70
Baron F. 2016. In *Astronomy at High Angular Resolution: A Compendium of Techniques in the Visible and Near-Infrared*, ed. HMJ Boffin, G Hussain, J-P Berger, L Schmidtobreick. *Ap. Space Sci. Libr.* 439:75–93. Cham, Switz.: Springer
Baron FR. 2020. *Proc. SPIE Conf. Ser.* 11446:114461N
Baudoin R, Darré P, Gomes JT, et al. 2016. *J. Astron. Instrum.* 5(3):1650006
Beckers JM. 1993. *Annu. Rev. Astron. Astrophys.* 31:13–62
Beckers JM, Enard D, Faucherre M, et al. 1990. *Proc. SPIE Conf. Ser.* 1236:108–24
Benisty M, Dominik C, Follette K, et al. 2022. arXiv:2203.09991
Benisty M, Natta A, Isella A, et al. 2010. *Astron. Astrophys.* 511:A74
Berger JP, Bourdarot G, Guillet de Chatellus H. 2020. *Proc. SPIE Conf. Ser.* 11446:1144613
Berger JP, Haguenauer P, Kern P, et al. 2001. *Astron. Astrophys.* 376:L31–34
Berger JP, Monnier JD, Millan-Gabet R, Renard S, Pedretti S. 2011. *Astron. Astrophys.* 529:L1
Bhatnagar S, Cornwell TJ, Golap K, Uson JM. 2008. *Astron. Astrophys.* 487:419–29
Bigioli A, Courney-Barrer B, Abuter R, et al. 2022. *Proc. SPIE Conf. Ser.* 12183:121831Z
Bland-Hawthorn J, Gerhard O. 2016. *Annu. Rev. Astron. Astrophys.* 54:529–96
Bland-Hawthorn J, Sellars MJ, Bartholomew JG. 2021. *J. Opt. Soc. Am. B* 38(7):A86–98
Böhm M, Glück M, Keck A, et al. 2017. *J. Opt. Soc. Am. A* 34(5):A10
Bohn AJ, Benisty M, Perraut K, et al. 2022. *Astron. Astrophys.* 658:A183
Bonnet H, Bauvir B, Wallander A, et al. 2006. *Messenger* 126:37–40
Born M, Wolf E. 1999. *Principles of Optics: Electromagnetic Theory of Propagation, Interference and Diffraction of Light*. Cambridge, UK: Cambridge Univ. Press. 7th ed.

Boskri A, Petrov RG, El Halkouj T, et al. 2021. *MNRAS* 506:1364–88
Bouvier J, Perraut K, Le Bouquin JB, et al. 2020. *Astron. Astrophys.* 636:A108
Boyajian TS, von Braun K, van Belle G, et al. 2012. *Ap. J.* 757(2):112
Boyd RW, Townes CH. 1977. *Appl. Phys. Lett.* 31(7):440–42
Bracewell RN. 1978. *Nature* 274(5673):780–81
Brown M, Thiel V, Allgaier M, et al. 2022. *Proc. SPIE Conf. Ser*. 12015:120150E
Brown RH, Twiss RQ. 1956. *Nature* 177(4497):27–29
Burtscher L, Meisenheimer K, Tristram KRW, et al. 2013. *Astron. Astrophys.* 558:A149
Buscher DF. 1994. In *Very High Angular Resolution Imaging, Proceedings of the 158th Symposium of the International Astronomical Union*, ed. JG Robertson, WJ Tango, pp. 91–93. Dordrecht, Neth.: Springer
Buscher DF. 2015. *Practical Optical Interferometry: Imaging at Visible and Infrared Wavelengths*. Cambridge, UK: Cambridge Univ. Press
Buscher DF, Creech-Eakman M, Farris A, et al. 2013. *J. Astron. Instrum.* 2(2):1340001
Cassan A, Ranc C, Absil O, et al. 2022. *Nat. Astron.* 6:121–28
Che X, Monnier JD, Zhao M, et al. 2011. *Ap. J.* 732(2):68
Cherenkov Telesc. Array Consort., Acharya BS, Agudo I, et al. 2019. *Science with the Cherenkov Telescope Array*. Singapore: World Sci.
Chiavassa A, Kravchenko K, Montargès M, et al. 2022. *Astron. Astrophys.* 658:A185
Chiavassa A, Plez B, Josselin E, Freytag B. 2009. *Astron. Astrophys.* 506(3):1351–65
Choquet É, Menu J, Perrin G, et al. 2014. *Astron. Astrophys.* 569:A2
Claes R, Kluska J, Van Winckel H, Min M. 2020. *Proc. SPIE Conf. Ser*. 11446:114461U
Claveau C-A, Bottom M, Jacobson S, et al. 2022. *Proc. SPIE Conf. Ser*. 12191:121910Z
Colavita MM. 2009. *New Astron. Rev.* 53(11–12):344–52
Colavita MM, Boden AF, Crawford SL, et al. 1998. *Proc. SPIE Conf. Ser*. 3350:776–84
Colavita MM, Booth AJ, Garcia-Gathright JI, et al. 2010. *Publ. Astron. Soc. Pac.* 122(893):795–807
Colavita MM, Serabyn E, Millan-Gabet R, et al. 2009. *Publ. Astron. Soc. Pac.* 121(884):1120–38
Colavita MM, Wallace JK, Hines BE, et al. 1999. *Ap. J.* 510:505–21
Colavita MM, Wizinowich PL. 2003. *Proc. SPIE Conf. Ser*. 4838:79–88
Colavita MM, Wizinowich PL, Akeson RL, et al. 2013. *Publ. Astron. Soc. Pac.* 125(932):1226–64
Conan JM, Rousset G, Madec PY. 1995. *J. Opt. Soc. Am. A* 12(7):1559–70
Coudé du Foresto V, Perrin G, Ruilier C, et al. 1998. *Proc. SPIE Conf. Ser*. 3350:856–63
Crawford SL, Ragland S, Booth A, et al. 2006. *Proc. SPIE Conf. Ser*. 6268:62683W
Danchi WC, Bester M, Degiacomi CG, Greenhill LJ, Townes CH. 1994. *Astron. J.* 107:1469–513
Davies R, Kasper M. 2012. *Annu. Rev. Astron. Astrophys.* 50:305–51
Davis J, Tango WJ, Booth AJ, et al. 1999. *MNRAS* 303(4):773–82
Defrère D, Absil O, Berger JP, et al. 2018. *Exp. Astron.* 46(3):475–95
Defrère D, Hinz PM, Mennesson B, et al. 2016. *Ap. J.* 824(2):66
Delplancke F. 2008. *New Astron. Rev.* 52(2–5):199–207
di Benedetto GP, Conti G. 1983. *Ap. J.* 268:309–18
Di Lieto N, Haguenauer P, Sahlmann J, Vasisht G. 2008. *Proc. SPIE Conf. Ser*. 7013:70130H
Do T, Hees A, Ghez A, et al. 2019. *Science* 365(6454):664–68
Dong S, Mérand A, Delplancke-Ströbele F, et al. 2019. *Ap. J.* 871:70
Dullemond CP, Monnier JD. 2010. *Annu. Rev. Astron. Astrophys.* 48:205–39
Duvert G, Young J, Hummel CA. 2017. *Astron. Astrophys.* 597:A8
Dyck HM, Benson JA, Ridgway ST. 1993. *Publ. Astron. Soc. Pac.* 105:610–15
Eisenhauer F. 2019. In *The Very Large Telescope in 2030 (VLT2030), ESO Garching, Germany, June 17–20*. **https://doi.org/10.5281/zenodo.3356274**
Eisenhauer F, Perrin G, Rabien S, et al. 2008. In *The Power of Optical/IR Interferometry: Recent Scientific Results and 2nd Generation Instrumentation*, ed. A Richichi, F Delplancke, F Paresce, A Chelli, pp. 431–44. Berlin/Heidelberg: Springer
Eisner JA, Graham JR, Akeson RL, Najita J. 2009. *Ap. J.* 692:309–23
Elhalkouj T, Ziad A, Petrov RG, et al. 2008. *Astron. Astrophys.* 477:337–44

Errmann R, Minardi S, Labadie L, et al. 2015. *Appl. Opt.* 54(24):7449–54
Ertel S, Defrère D, Hinz P, et al. 2020. *Astron. J.* 159(4):177
Espinosa Lara F, Rieutord M. 2013. *Astron. Astrophys.* 552:A35
Event Horizon Telesc. Collab., Akiyama K, Alberdi A, et al. 2022. *Ap. J. Lett.* 930(2):L12
Feautrier P, Gach JL, Guieu S, et al. 2014. *Proc. SPIE Conf. Ser*. 9148:914818
Feautrier P, Gach JL, Owton D, et al. 2022. *Proc. SPIE Conf. Ser*. 12191:121911R
Ferrari M, Lemaitre GR, Mazzanti SP, et al. 2003. *Proc. SPIE Conf. Ser*. 4838:1155–62
Finger G, Baker I, Alvarez D, et al. 2016. *Proc. SPIE Conf. Ser*. 9909:990912
Finger G, Baker I, Alvarez D, et al. 2019. *Proc. SPIE Conf. Ser*. 11180:111806L
Finger G, Baker I, Dorn R, et al. 2010. *Proc. SPIE Conf. Ser*. 7742:77421K
Finger G, Baker I, Downing M, et al. 2017. *Proc. SPIE Conf. Ser*. 10563:1056311
Finger G, Eisenhauer F, Hardy T, et al. 2022. *Proc. SPIE Conf. Ser*. 12191:121911S
Fizeau H. 1868. *C. R. Acad. Sci.* 66:932–34
Froehly C. 1981. In *Scientific Importance of High Angular Resolution at Infrared and Optical Wavelengths*, ed. MH Ulrich, K Kjär, pp. 285–93. Garching, Ger.: ESO
Gai M, Corcione L, Lattanzi MG, et al. 2003. *Mem. Soc. Astron. Ital.* 74:472–73
Gaia Collab., Prusti T, de Bruijne JHJ, et al. 2016. *Astron. Astrophys.* 595:A1
Gallenne A, Mérand A, Kervella P, et al. 2015. *Astron. Astrophys.* 579:A68
Gámez Rosas V, Isbell JW, Jaffe W, et al. 2022. *Nature* 602(7897):403–7
Garcia EV, Muterspaugh MW, van Belle G, et al. 2016. *Publ. Astron. Soc. Pac.* 128(963):055004
Gardner T, Monnier JD, Fekel FC, et al. 2021. *Astron. J.* 161:40
Gardner T, Monnier JD, Fekel FC, et al. 2022. *Astron. J.* 164:184
Genzel R, Eisenhauer F, Gillessen S. 2010. *Rev. Mod. Phys.* 82(4):3121–95
Gitton PB, Leveque SA, Avila G, Phan Duc T. 2004. *Proc. SPIE Conf. Ser.* 5491:944–53
Glindemann A. 2011. *Principles of Stellar Interferometry*. Berlin/Heidelberg: Springer-Verlag
Goebel SB, Hall DNB, Guyon O, et al. 2018. *J. Astron. Telesc. Instrum. Syst.* 4(2):026001
Gottesman D, Jennewein T, Croke S. 2012. *Phys. Rev. Lett.* 109(7):070503
GRAVITY Collab., Abuter R, Accardo M, et al. 2017a. *Astron. Astrophys.* 602:A94
GRAVITY Collab., Abuter R, Aimar N, et al. 2022a. *Astron. Astrophys.* 657:A82
GRAVITY Collab., Abuter R, Aimar N, et al. 2022b. *Astron. Astrophys.* 657:L12
GRAVITY Collab., Abuter R, Allouche F, et al. 2022c. *Astron. Astrophys.* 665:A75
GRAVITY Collab., Abuter R, Amorim A, et al. 2018a. *Astron. Astrophys.* 615:L15
GRAVITY Collab., Abuter R, Amorim A, et al. 2018b. *Astron. Astrophys.* 618:L10
GRAVITY Collab., Abuter R, Amorim A, et al. 2019a. *Astron. Astrophys.* 625:L10
GRAVITY Collab., Abuter R, Amorim A, et al. 2020a. *Astron. Astrophys.* 638:A2
GRAVITY Collab., Abuter R, Amorim A, et al. 2020b. *Astron. Astrophys.* 636:L5
GRAVITY Collab., Abuter R, Amorim A, et al. 2021a. *Astron. Astrophys.* 645:A127
GRAVITY Collab., Abuter R, Amorim A, et al. 2021b. *Astron. Astrophys.* 647:A59
GRAVITY Collab., Amorim A, Bauböck M, et al. 2020c. *Astron. Astrophys.* 643:A154
GRAVITY Collab., Amorim A, Bauböck M, et al. 2021c. *Astron. Astrophys.* 648:A117
GRAVITY Collab., Amorim A, Bauböck M, et al. 2021d. *Astron. Astrophys.* 654:A85
GRAVITY Collab., Caratti o Garatti A, Fedriani R, et al. 2020d. *Astron. Astrophys.* 635:L12
GRAVITY Collab., Dexter J, Shangguan J, et al. 2020e. *Astron. Astrophys.* 635:A92
GRAVITY Collab., Garcia Lopez R, Natta A, et al. 2020f. *Nature* 584(7822):547–50
GRAVITY Collab., Lacour S, Nowak M, et al. 2019b. *Astron. Astrophys.* 623:L11
GRAVITY Collab., Nowak M, Lacour S, et al. 2020g. *Astron. Astrophys.* 633:A110
GRAVITY Collab., Perraut K, Labadie L, et al. 2019c. *Astron. Astrophys.* 632:A53
GRAVITY Collab., Perraut K, Labadie L, et al. 2021e. *Astron. Astrophys.* 655:A73
GRAVITY Collab., Petrucci PO, Waisberg I, et al. 2017b. *Astron. Astrophys.* 602:L11
GRAVITY Collab., Pfuhl O, Davies R, et al. 2020h. *Astron. Astrophys.* 634:A1
GRAVITY Collab., Sanchez-Bermudez J, Caratti o Garatti A, et al. 2021f. *Astron. Astrophys.* 654:A97
GRAVITY Collab., Sturm E, Dexter J, et al. 2018c. *Nature* 563(7733):657–60

GRAVITY Collab., Wojtczak JA, Labadie L, et al. 2023. *Astron. Astrophys.* 669:A59
Guerin W, Dussaux M, Fouche M, et al. 2017. *MNRAS* 472:4126–32
Guesalaga A, Neichel B, Rigaut F, et al. 2012. *Appl. Opt.* 51(19):4520–35
Gull SF, Skilling J. 1984. In *Indirect Imaging: Measurement and Processing for Indirect Imaging*, ed. JA Roberts, pp. 219–25. Cambridge, UK: Cambridge Univ. Press
Guyon O, Mennesson B, Serabyn E, Martin S. 2013. *Publ. Astron. Soc. Pac.* 125(930):951–65
Hale DDS, Bester M, Danchi WC, et al. 2000. *Ap. J.* 537(2):998–1012
Hanbury Brown R, Davis J, Allen LR. 1967. *MNRAS* 137:375–92
Hansen JT, Ireland MJ, LIFE Collab. 2022. *Astron. Astrophys.* 664:A52
Hartmann L, Kenyon SJ. 1985. *Ap. J.* 299:462–78
Haubois X, Perrin G, Lacour S, et al. 2009. *Astron. Astrophys.* 508(2):923–32
Hillen M, Kluska J, Le Bouquin JB, et al. 2016. *Astron. Astrophys.* 588:L1
Hinkley S, Lacour S, Marleau GD, et al. 2023. *Astron. Astrophys.* 671:L5
Hinz PM, Angel JRP, Hoffmann WF, et al. 1998. *Nature* 395(6699):251–53
Hippler S, Brandner W, Scheithauer S, et al. 2020. *Instruments* 4(3):20
Hofmann KH, Weigelt G, Schertl D. 2014. *Astron. Astrophys.* 565:A48
Högbom JA. 1974. *Astron. Astrophys. Suppl.* 15:417–26
Hönig SF, Watson D, Kishimoto M, Hjorth J. 2014. *Nature* 515(7528):528–30
Horch EP, van Belle G, Genet RM, Holenstein BD. 2013. *J. Astron. Instrum.* 2(2):1340009
Hsiao HK, Winick KA, Monnier JD. 2010. *Appl. Opt.* 49(35):6675–88
Hsiao HK, Winick KA, Monnier JD, Berger JP. 2009. *Opt. Express* 17(21):18489–500
Huber D, Ireland MJ, Bedding TR, et al. 2012. *Ap. J.* 760:32
Ibrahim N, Monnier JD, Kraus S, et al. 2023. *Ap. J.* 947:68
Ireland MJ, Mérand A, ten Brummelaar TA, et al. 2008. *Proc. SPIE Conf. Ser.* 7013:701324
Ireland MJ, Monnier JD. 2014. *Proc. SPIE Conf. Ser.* 9146:914612
Ireland MJ, Monnier JD, Thureau N. 2006. *Proc. SPIE Conf. Ser.* 6268:62681T
Ireland MJ, Woillez J. 2021. In *The WSPC Handbook of Astronomical Instrumentation*, Vol. 3, *UV, Optical & IR Instrumentation: Part 2*, ed. AM Moore, pp. 103–26. Singapore: World Sci.
Jaffe W, Meisenheimer K, Röttgering HJA, et al. 2004. *Nature* 429(6987):47–49
Jennison RC. 1958. *MNRAS* 118:276–84
Johnson MA, Betz AL, Townes CH. 1974. *Phys. Rev. Lett.* 33(27):1617–20
Kalman RE. 1960. *Trans. ASME–J. Basic Eng.* 82(Ser. D):35–45
Kasper JC, Lazio J, Romero-Wolf A, et al. 2019. Fall Meeting, Am. Geophys. Union. Abstr. #SH33A–02
Kellerer A, Tokovinin A. 2007. *Astron. Astrophys.* 461(2):775–81
Kenchington Goldsmith HD, Cvetojevic N, Ireland M, Madden S. 2017. *Opt. Express* 25(4):3038–51
Kern P, Malbet F, Schanen-Duport I, Benech P. 1997. In *Integrated Optics for Astronomical Interferometry*, Vol. 115, ed. P Kern, F Malbet, pp. 195–203. Grenoble, Fr.: Bastianelli-Guirimand
Kishimoto M, Hönig SF, Antonucci R, et al. 2011. *Astron. Astrophys.* 527:A121
Kloppenborg B, Stencel R, Monnier JD, et al. 2010. *Nature* 464(7290):870–872
Kluska J, Berger JP, Malbet F, et al. 2020a. *Astron. Astrophys.* 636:A116
Kluska J, Malbet F, Berger JP, et al. 2014. *Astron. Astrophys.* 564:A80
Kluska J, Olofsson H, Van Winckel H, et al. 2020b. *Astron. Astrophys.* 642:A152
Kobus J, Wolf S, Ratzka T, Brunngräber R. 2020. *Astron. Astrophys.* 642:A104
Koechlin L, Rabbia Y. 1985. *Astron. Astrophys.* 153:91–98
Kok Y, Ireland MJ, Tuthill PG, et al. 2013. *J. Astron. Instrum.* 2(2):1340011
Koshida S, Minezaki T, Yoshii Y, et al. 2014. *Ap. J.* 788(2):159
Kraus S, Hofmann KH, Benisty M, et al. 2008. *Astron. Astrophys.* 489(3):1157–73
Kraus S, Kreplin A, Young AK, et al. 2020a. *Science* 369(6508):1233–38
Kraus S, Le Bouquin JB, Kreplin A, et al. 2020b. *Ap. J. Lett.* 897:L8
Kraus S, Mortimer D, Chhabra S, et al. 2022. *Proc. SPIE Conf. Ser.* 12183:121831S
Kulcsár C, Massioni P, Sivo G, Raynaud HFG. 2012. *Proc. SPIE Conf. Ser.* 8447:84470Z
Labadie L, Minardi S, Martín G, Thomson RR. 2018. *Exp. Astron.* 46(3):433–45

Labdon A, Kraus S, Davies CL, et al. 2019. *Astron. Astrophys.* 627:A36
Labdon A, Kraus S, Davies CL, et al. 2021. *Astron. Astrophys.* 646:A102
Labeyrie A. 1975. *Ap. J. Lett.* 196:L71–75
Labeyrie A. 1996. *Astron. Astrophys. Suppl. Ser.* 118:517–524
Labeyrie A, Lipson SG, Nisenson P. 2014. *An Introduction to Optical Stellar Interferometry*. Cambridge, UK: Cambridge Univ. Press
Lacour S, Dembet R, Abuter R, et al. 2019. *Astron. Astrophys.* 624:A99
Lacour S, Eisenhauer F, Gillessen S, et al. 2014a. *Proc. SPIE Conf. Ser*. 9146:91462E
Lacour S, Tuthill P, Monnier JD, et al. 2014b. *MNRAS* 439(4):4018–29
Lacour S, Wang JJ, Rodet L, et al. 2021. *Astron. Astrophys.* 654:L2
Lagrange AM, Rubini P, Nowak M, et al. 2020. *Astron. Astrophys.* 642:A18
Lane BF, Colavita MM. 2003. *Astron. J.* 125(3):1623–28
Lawson PR. 2000a. See Lawson 2000b, pp. 113–42
Lawson PR, ed. 2000b. *Principles of Long Baseline Stellar Interferometry, Course Notes from the 1999 Michelson Summer School, August 15–19, 1999*. Pasadena, CA: JPL
Lawson PR, Cotton WD, Hummel CA, et al. 2004. *Proc. SPIE Conf. Ser*. 5491:886–99
Lazareff B, Berger JP, Kluska J, et al. 2017. *Astron. Astrophys.* 599:A85
Lazareff B, Blind N, Jocou L, et al. 2014. *Proc. SPIE Conf. Ser*. 9146:91460X
Le Besnerais G, Lacour S, Mugnier LM, et al. 2008. *IEEE J. Sel. Top. Signal Proc.* 2(5):767–80
Le Bouquin JB, Berger JP, Lazareff B, et al. 2011. *Astron. Astrophys.* 535:A67
Le Bouquin JB, Lacour S, Renard S, et al. 2009. *Astron. Astrophys.* 496:L1–4
Leftley JH, Tristram KRW, Hönig SF, et al. 2021. *Ap. J.* 912(2):96
Léna P. 1979. *J. Opt.* 10:323–28
Léna P. 2020. *Astronomy's Quest for Sharp Images*. Cham, Switz.: Springer
Leveque SA, Wilhelm R, Salvade Y, Scherler O, Daendliker R. 2003. *Proc. SPIE Conf. Ser*. 4838:983–94
Lindegren L. 1980. *Astron. Astrophys.* 89(1–2):41–47
Lippa M, Gillessen S, Blind N, et al. 2016. *Proc. SPIE Conf. Ser*. 9907:990722
Lohmann AW, Weigelt G, Wirnitzer B. 1983. *Appl. Opt.* 22:4028–37
Lopez B, Lagarde S, Petrov RG, et al. 2022. *Astron. Astrophys.* 659:A192
Lu RS, Broderick AE, Baron F, et al. 2014. *Ap. J.* 788(2):120
Lynden-Bell D, Rees MJ. 1971. *MNRAS* 152:461–75
Martinez AO, Baron FR, Monnier JD, et al. 2021. *Ap. J.* 916:60
Martinod MA, Tuthill P, Gross S, et al. 2021. *Appl. Opt.* 60(19):D100
Matsuo T, Ikari S, Kondo H, et al. 2022. *J. Astron. Telesc. Instrum. Syst.* 8:015001
Mawet D, Pueyo L, Lawson P, et al. 2012. *Proc. SPIE Conf. Ser*. 8442:844204
McAlister HA. 2020. *Proc. SPIE Conf. Ser*. 11446:1144604
Mennesson B, Hanot C, Serabyn E, et al. 2011. *Ap. J.* 743(2):178
Mennesson B, Millan-Gabet R, Serabyn E, et al. 2014. *Ap. J.* 797(2):119
Menu J, Perrin G, Choquet E, Lacour S. 2012. *Astron. Astrophys.* 541:A81
Mérand A. 2022. Astrophysics Source Code Library. ascl:2205.001
Merkle F, Léna P. 1986. *Proc. SPIE Conf. Ser.* 0628:261–72
Michelson AA. 1891. *Nature* 45(1155):160–61
Michelson AA, Pease FG. 1921. *Ap. J.* 53:249–59
Millan-Gabet R, Schloerb FP, Traub WA, Carleton NP. 1999. *Publ. Astron. Soc. Pac.* 111(756):238–45
Millan-Gabet R, Serabyn E, Mennesson B, et al. 2011. *Ap. J.* 734:67
Mollière P, Stolker T, Lacour S, et al. 2020. *Astron. Astrophys.* 640:A131
Monnier J, Aarnio A, Absil O, et al. 2019. *Bull. Am. Astron. Soc.* 51:153
Monnier JD. 2000. See Lawson 2000b, pp. 203–30
Monnier JD. 2003. *Rep. Prog. Phys.* 66(5):789–857
Monnier JD, Baron F, Anderson M, et al. 2012. *Proc. SPIE Conf. Ser*. 8445:84451I
Monnier JD, Berger JP, Le Bouquin JB, et al. 2014. *Proc. SPIE Conf. Ser*. 9146:91461Q
Monnier JD, Ireland M, Kraus S, et al. 2018. *Proc. SPIE Conf. Ser*. 10701:1070118

Monnier JD, Millan-Gabet R. 2002. *Ap. J.* 579(2):694–98
Monnier JD, Zhao M, Pedretti E, et al. 2007. *Science* 317(5836):342
Montargès M, Cannon E, Lagadec E, et al. 2021. *Nature* 594(7863):365–68
Mortimer DJ, Buscher DF. 2022. *MNRAS* 511(3):4619–32
Mourard D, Monnier JD, Meilland A, et al. 2015. *Astron. Astrophys.* 577:A51
Mourard D, Nardetto N, ten Brummelaar T, et al. 2018. *Proc. SPIE Conf. Ser*. 10701:1070120
Mourard D, Tallon-Bosc I, Blazit A, et al. 1994. *Astron. Astrophys.* 283(2):705–13
Mozurkewich D, Armstrong JT, Hindsley RB, et al. 2003. *Astron. J.* 126:2502–20
Muterspaugh MW, Lane BF, Konacki M, et al. 2006. *Ap. J.* 636(2):1020–32
Muterspaugh MW, Lane BF, Kulkarni SR, et al. 2010. *Astron. J.* 140(6):1657–71
Netzer H. 2015. *Annu. Rev. Astron. Astrophys.* 53:365–408
Nowak M, Lacour S, Lagrange AM, et al. 2020. *Astron. Astrophys.* 642:L2
Nuñez PD, Holmes R, Kieda D, Rou J, LeBohec S. 2012. *MNRAS* 424(2):1006–11
Ohnaka K, Weigelt G, Hofmann KH. 2017. *Nature* 548(7667):310–12
Paladini C, Baron F, Jorissen A, et al. 2018. *Nature* 553(7688):310–12
Pancoast A, Brewer BJ, Treu T, et al. 2014. *MNRAS* 445(3):3073–91
Parks JR, White RJ, Baron F, et al. 2021. *Ap. J.* 913:54
Pauls TA, Young JS, Cotton WD, Monnier JD. 2005. *Publ. Astron. Soc. Pac.* 117(837):1255–62
Paumard T, Perrin G, Eckart A, et al. 2008. In *The Power of Optical/IR Interferometry: Recent Scientific Results and 2nd Generation Instrumentation*, ed. A Richichi, F Delplancke, F Paresce, A Chelli, pp. 313–17. Berlin/Heidelberg: Springer
Pease FG. 1930. *Sci. Am.* 143(4):290–93
Pease FG. 1931. In *Ergebnisse der Exakten Naturwissenschaften*, Vol. 10, pp. 84–96. Berlin: Springer
Perraut K, Dougados C, Lima GHRA, et al. 2016. *Astron. Astrophys.* 596:A17
Perraut K, Jocou L, Berger JP, et al. 2018. *Astron. Astrophys.* 614:A70
Perrin G, Coudé du Foresto V, Ridgway ST, et al. 1998. *Publ. Astron. Soc. Pac.* 154:2021–28
Perrin G, Ridgway ST, Lacour S, et al. 2020. *Astron. Astrophys.* 642:A82
Perrin G, Ridgway ST, Mennesson B, et al. 2004. *Astron. Astrophys.* 426:279–96
Perrin G, Woillez J. 2019. *Astron. Astrophys.* 625:A48
Quanz SP, Ottiger M, Fontanet E, et al. 2022. *Astron. Astrophys.* 664:A21
Quirrenbach A. 2000. See Lawson 2000b, pp. 143–162
Quirrenbach A. 2001. *Annu. Rev. Astron. Astrophys.* 39:353–401
Readhead ACS, Wilkinson PN. 1978. *Ap. J.* 223:25–36
Renard S, Thiébaut E, Malbet F. 2011. *Astron. Astrophys.* 533:A64
Richardson ND, Lee L, Schaefer G, et al. 2021. *Ap. J. Lett.* 908:L3
Righini GC, Chiappini A. 2014. *Opt. Eng.* 53:071819
Roddier F. 1981. *Prog. Opt.* 19:281–376
Roettenbacher RM, Monnier JD, Korhonen H, et al. 2016. *Nature* 533(7602):217–20
Rousset G, Fontanella JC, Kern P, Gigan P, Rigaut F. 2001. *Astron. Astrophys.* 230:L29–32
Rubilar GF, Eckart A. 2001. *Astron. Astrophys.* 374:95–104
Ryle M, Hewish A. 1960. *MNRAS* 120:220–30
Sana H, Le Bouquin JB, Lacour S, et al. 2014. *Ap. J. Suppl.* 215:15
Sargent AI, Welch WJ. 1993. *Annu. Rev. Astron. Astrophys.* 31:297–343
Schaefer GH, Brummelaar TT, Gies DR, et al. 2014. *Nature* 515(7526):234–36
Schöller M. 2007. *New Astron. Rev.* 51(8–9):628–38
Serabyn E, Mennesson B, Colavita MM, et al. 2012. *Ap. J.* 748:55
Setterholm BR, Monnier JD, Davies CL, et al. 2018. *Ap. J.* 869(2):164
Setterholm BR, Monnier JD, Le Bouquin J-B, et al. 2022. *Proc. SPIE Conf. Ser*. 12183:121830B
Shaklan SB, Roddier F. 1987. *Appl. Opt.* 26:2159–63
Shao M, Colavita MM. 1992. *Astron. Astrophys.* 262:353–58
Shao M, Colavita MM, Hines BE, et al. 1988. *Astron. Astrophys.* 193(1–2):357–71
Shao M, Staelin DH. 1977. *J. Opt. Soc. Am.* 67:81–86

Shao M, Staelin DH. 1980. *Appl. Opt.* 19:1519–22
Stephan ECR. 1874. *C. R. Acad. Sci.* 78:1008–12
Swain M, Vasisht G, Akeson R, et al. 2003. *Ap. J. Lett.* 596(2):L163–66
ten Brummelaar TA, McAlister HA, Ridgway ST, et al. 2005. *Ap. J.* 628:453–65
ten Brummelaar TA, Sturmann L, Sturmann J, et al. 2012. *Proc. SPIE Conf. Ser*. 8447:84473I
Thiébaut E. 2008. *Proc. SPIE Conf. Ser*. 7013:70131I
Thiébaut É, Young J. 2017. *J. Opt. Soc. Am. A* 34(6):904
Thompson AR, Moran JM, Swenson GW Jr. 2017. *Interferometry and Synthesis in Radio Astronomy*. Cham, Switz.: Springer. 3rd ed.
Townes CH. 2000. See Lawson 2000b, pp. 59–70
Traub WA, Ahearn A, Carleton NP, et al. 2003. *Proc. SPIE Conf. Ser*. 4838:45–52
van Belle GT. 2012. *Astron. Astrophys. Rev.* 20:51
Vasisht G, Booth AJ, Colavita MM, et al. 2003. *Proc. SPIE Conf. Ser*. 4838:824–34
Waisberg I, Dexter J, Pfuhl O, et al. 2017. *Ap. J.* 844:72
Wallace AL, Ireland MJ, Federrath C. 2021. *MNRAS* 508(2):2515–23
Wang JJ, Vigan A, Lacour S, et al. 2021. *Astron. J.* 161(3):148
Wang JM, Songsheng YY, Li YR, et al. 2020. *Nat. Astron.* 4:517–25
Wizinowich PL, Acton DS, Lai O, et al. 2000. *Proc. SPIE Conf. Ser*. 4007:2–13
Woillez J, Abad JA, Abuter R, et al. 2019. *Astron. Astrophys.* 629:A41
Woillez J, Akeson R, Colavita M, et al. 2010. *Proc. SPIE Conf. Ser*. 7734:773412
Woillez J, Akeson R, Colavita M, et al. 2012. *Publ. Astron. Soc. Pac.* 124(911):51–61
Woillez J, Darré P, Egner S, et al. 2018. *Proc. SPIE Conf. Ser*. 10701:1070103
Woillez J, Lacour S. 2013. *Ap. J.* 764:109
Woillez J, Wizinowich P, Akeson R, et al. 2014. *Ap. J.* 783(2):104
Zang W, Dong S, Gould A, et al. 2020. *Ap. J.* 897(2):180
Zhao M, Gies D, Monnier JD, et al. 2008. *Ap. J. Lett.* 684(2):L95–98
Ziad A. 2016. *Proc. SPIE Conf. Ser*. 9909:99091K